The Influence of Solar System Oscillation on the Variability of the Total Solar Irradiance

Article · August 2016

DOI: 10.1016/j.newast.2016.08.020

2 authors:

Harald Yndestad
Norwegian University of Science and Technol…
51 PUBLICATIONS **234** CITATIONS
SEE PROFILE

J.-E. Solheim
University of Tromsoe
211 PUBLICATIONS **1,785** CITATIONS
SEE PROFILE

New Astronomy 51 (2017) 135–152

Contents lists available at ScienceDirect

New Astronomy

journal homepage: www.elsevier.com/locate/newast

The influence of solar system oscillation on the variability of the total solar irradiance

Harald Yndestad [a,*], Jan-Erik Solheim [b,1]

[a] Norwegian University of Science and Technology Aalesund, Aalesund 6025, Norway
[b] Department of Physics and Technology UiT The Arctic, University of Norway, Tromsø 9037, Norway

HIGHLIGHTS

- Deterministic TSI periods
- TSI variability control by large planets
- Next Dalton TSI minimum

ARTICLE INFO

Article history:
Received 12 March 2016
Revised 28 August 2016
Accepted 29 August 2016
Available online 30 August 2016

Keywords:
Solar oscillation
Solar irradiation oscillation
Wavelet analysis
Grand minima

ABSTRACT

Total solar irradiance (TSI) is the primary quantity of energy that is provided to the Earth. The properties of the TSI variability are critical for understanding the cause of the irradiation variability and its expected influence on climate variations. A deterministic property of TSI variability can provide information about future irradiation variability and expected long-term climate variation, whereas a non-deterministic variability can only explain the past.

This study of solar variability is based on an analysis of two TSI data series, one since 1700 A.D. and one since 1000 A.D.; a sunspot data series since 1610 A.D.; and a solar orbit data series from 1000 A.D. The study is based on a wavelet spectrum analysis. First, the TSI data series are transformed into a wavelet spectrum. Then, the wavelet spectrum is transformed into an autocorrelation spectrum to identify stationary, subharmonic and coincidence periods in the TSI variability.

The results indicate that the TSI and sunspot data series have periodic cycles that are correlated with the oscillations of the solar position relative to the barycenter of the solar system, which is controlled by gravity force variations from the large planets Jupiter, Saturn, Uranus and Neptune. A possible explanation for solar activity variations is forced oscillations between the large planets and the solar dynamo.

We find that a stationary component of the solar variability is controlled by the 12-year Jupiter period and the 84-year Uranus period with subharmonics. For TSI and sunspot variations, we find stationary periods related to the 84-year Uranus period. Deterministic models based on the stationary periods confirm the results through a close relation to known long solar minima since 1000 A.D. and suggest a modern maximum period from 1940 to 2015. The model computes a new Dalton-type sunspot minimum from approximately 2025 to 2050 and a new Dalton-type period TSI minimum from approximately 2040 to 2065.

1. Introduction

Total solar irradiance (TSI) is the primary source of energy that is provided to the Earth's climate system. A variation in TSI will contribute to a natural climate variation on the Earth. TSI has varied approximately 0.3% over the past 300 years (Scafetta and Willson, 2014). A better understanding of the TSI variability properties is critical for understanding the cause of its variability. A TSI data series has information that reflects the cause of the TSI variability. If the TSI variability has deterministic oscillating periods, then we can forecast expected TSI variations, whereas a random TSI variability can only explain the past. The intermittency of the solar variation is preferably explained as stochastic noise (Charbonneu, 2010). In this investigation, we introduce a simple hypothesis: if the TSI variability has a periodic oscillation, then this

* Corresponding author. Fax: +47 70161300.
E-mail address: harald.yndestad@ntnu.no (H. Yndestad).
[1] Retired, Current Address: Wilh. Wilhelmsen v 71, 1362 Hosle, Norway

http://dx.doi.org/10.1016/j.newast.2016.08.020
1384-1076/

oscillation must have a source that influences the solar energy oscillation. A possible source is the variable distance to the planets, which create oscillating tidal effects, which we refer to as gravity oscillations (GOs).

1.1. Solar variability

The assumption that solar activity were immutable, as postulated by Aristotle (384-322 B.C.), was believed for millenia in numerous societies (cf: Usoskin (2013)). Although some transient changes of the Sun were observed with the naked eye, the introduction of the telescope in approximately 1600 demonstrated that the Sun possessed spots that varied in number and location. From 1610, systematic observations were reported. A pattern of sunspot variations was established when Heinrich Schwabe began regular observations of sunspots in 1826. He reported a possible period of approximately ten years (Schwabe, 1844). Wolf (1859) presented the opinion that the planets Venus, Earth, Jupiter and Saturn modulate the solar variability.

The solar activity cycle (Hathaway, 2015) consists of dark sunspots and bright regions (faculae) in addition to active regions that exhibit sudden energy releases (flares). The average cycle length is 11.1 years. During a cycle, the number of spots increases to a maximum and then decreases. The average lifetime of a sunspot is slightly longer than the solar rotation period. They are bipolar, with the same magnetic polarity that leads with respect to the direction of the solar rotation. When the next cycle starts, spots appear with opposite polarity at high latitudes in both hemispheres, and as the cycle progress, they appear closer to the equator.

The 11.1-year sunspot period is referred to as the Schwabe cycle, and it is proposed to be created by the tidal torque from the planets Venus, Earth and Jupiter (Wilson, 2013). The 22-year magnetic reversal period is referred to as the Hale period. Scafetta (2012a); 2012b) showed that the 11-year Schwabe sunspot cycle consists of three periods of 9.98, 10.90 and 11.86 years, which are close to the Jupiter/Saturn spring period of 9.93 years; a tidal pattern of Venus, Earth and Jupiter of 11.07 years; and the Jupiter orbital period of 11.86 years. A simplified harmonic model based on these 3 periods produces a complex quasi-periodic interference/beat pattern. The major beat periods occur at approximately 115, 61 and 130 years, in addition to a quasi-millennial large beat cycle of approximately 983 years. The harmonic model hindcasts solar minima and maxima from the last hundred years, the grand minima over the last millennium, and explains the global surface temperature modulation since 1850 (Scafetta, 2012a; 2012b). Solheim (2013) found that the 10.90 year period contained two periods (10.66 and 11.01 years), which was also shown to have a planetary origin (Scafetta, 2014a).

A relation between the planet and sunspot periods indicates the possibility of a deterministic long-term relation between planet periods and periods in sunspot data series.

1.1.1. Sunspot data series

The sunspot number time series is a measure of the long-term evolution of the solar cycle and a proxy for the long-term influence of the Sun on the Earth's climate. The relative sunspot number (R) as defined by Wolf (1861) is based on the total number of individual sunspots n and the number of sunspot groups g according to the formula $R = k(10g + n)$, where k is a correction factor for each observer. This parameter was introduced to correct for the use of different telescopes and observers. R is referred to as the Zürich, Wolf or International Sunspot Number. At present, SN is used for the International Sunspot Number (Clette et al., 2014).

Rudolf Wolf started systematic observations of sunspot numbers in 1849. He also collected previous observations to construct daily sunspot numbers from 1750 and a yearly series from 1700. The cycle that started in 1755 became sunspot cycle 1. The sunspot numbers had to be scaled upward several times due to missing spots. By approximately doubling the number of recovered observations and cleverly interpolating between sparse observations (Hoyt et al., 1994), gaps were reduced and the series was extended to the first recording of sunspots by telescope in 1610. The history of the sunspot series and the last extensive corrections are described by Clette et al. (2014). The revised yearly series, which is available from the World Data Center SILSO from July 2015, was employed in our analysis.

Because the standard sunspot series is a composite time series based on single spots and groups, the accuracy significantly decreases when going back in time. Due to poorer telescopes and locations, smaller spots were difficult to observe and frequently lost. To correct for this situation, Hoyt and Schatten (1998a; 1998b) constructed a new group sunspot number R_G that was normalized to the Zürich sunspot number. Their series covered the period 1610–1995 and was based on a larger and more refined observational database. Although the group sunspot number corresponded to the relative sunspot number in the 20th century, the maximum group number was 40% lower in the 19th century and previous centuries (Clette et al., 2014). The group sunspot numbers were recently revised, and the difference between the series may now be considered as random noise. However, during the last two sunspot cycles (nos. 23 and 24), 30% fewer sunspots per group were observed, which may be a sign of changes in the solar dynamo (Clette et al., 2014).

1.1.2. Solar activity periods – grand maxima and minima

In the 1890s, G. Spörer and E. W. Maunder (Maunder, 1890) reported that the solar activity was strongly reduced over a period of 70 years from 1645 to 1715 (Eddy, 1976; 1983). Based on naked-eye observations of sunspots, records of aurora activity, and a relation between ^{14}C variations and solar activity, a grand maximum (1100–1250) and the Spörer minimum (1460–1550) were also identified (Eddy, 1976).

The distribution of the solar activity can be interpreted as bimodal, which implies distinct modes of activity. The main (regular) mode corresponds to moderate activity, which has a maxima of the 10-yr average spot number between 20 spots and 67 spots. In addition, we obtain grand maxima and grand minima that are above this range and below this range, respectively (Usoskin, 2014). Studies that employ cosmogenic isotope data and sunspot data indicate that we are currently leaving a grand activity maximum, which began in approximately 1940 and is now declining (Usoskin et al., 2003; Solanki et al., 2004; Abreu et al., 2008).

Because grand maxima and minima occur on centennial or millennial timescales, they can only be investigated using proxy data, i.e., solar activity reconstructed from ^{10}Be and ^{14}C time-calibrated data. The conclusion is that the activity level of the Modern Maximum (1940–2000) is a relatively rare event, with the previous similarly high levels of solar activity observed 4 and 8 millennia ago (Usoskin et al., 2003). Nineteen grand maxima have been identified by Usoskin et al. (2007) in an 11,000-yr series.

Grand minimum modes with reduced activity cannot be explained by only random fluctuations of the regular mode (Usoskin, 2014). They can be characterized as two types: short minima in the length range of 50–80 years (Maunder-type) and longer minima (Spörer-type). Twenty-seven grand minima are identified with a total duration of 1900 years, or approximately 17% of the time during the past 11,500 years (Usoskin et al., 2007). An adjustment-free reconstruction of the solar activity over the last three millennia confirms four grand minima since the year 1000: Maunder (1640–1720), Spörer (1390–1550), Wolf (1270–1340) and Oort (1010–1070) (Usoskin et al., 2007). The Dalton minimum

(1790–1820) does not fit the definition of a grand minimum; it is more likely a regular deep minimum that is observed once per century or an immediate state between the grand minimum and normal activity (Usoskin, 2013).

Temperature reconstructions for the last millennium for the Northern Hemisphere (Ljungquist, 2010) show a medieval maximum temperature at approximately the year 1000 and a cooling period starting at approximately 1350, immediately after the Wolf minimum and lasting nearly 500 years, with the coldest period in what is referred to as the Little Ice Age (LIA) at the time of the Maunder minimum. A cold period was also observed during the time of the Dalton minimum. The Maunder and the Dalton minima are associated with less solar activity and colder climate periods. In this investigation, minimum solar activity periods may serve as a reference for the identified minimum irradiations in the TSI oscillations.

1.2. Total solar irradiance

Total solar irradiance (TSI) represents a direct index for the luminosity of the Sun measured at the average distance of the Earth. The solar luminosity was previously considered to be constant, and the TSI was named the solar constant. Since the beginning of satellite observations in 1979, the TSI has increased by approximately 0.1% from the solar minima to the solar maxima in the three satellite-observed sunspot cycles. The variation in the TSI level does not adequately explain the observed variations in the global temperature. In addition to the direct effect, however, many indirect effects exist, such as UV energy changes that affect the production of ozone, solar wind modulation of the galactic cosmic ray flux that may affect the formation of clouds, and local and regional effects on temperature, pressure, precipitation (monsoons) and ocean currents. The Pacific Decadal Oscillation (PDO) and the North Atlantic Oscillation (NAO) also show variations that are related to the phase of the TSI (Velasco and Mendoza, 2008). A significant relation between sunspots and ENSO data has also been observed (Hassan, 2016).

Composite TSI records have been constructed from a database of seven independent measurement series that cover different periods since 1979. Different approaches to the selection of results and cross-calibration have produced composites with different characteristics: the Active Cavity Radiometer Irradiance Monitor (ACRIM) and the Physikalisch-Meteorologisches Observatorium Davos (PMOD) series. The ACRIM composite uses the TSI measurements that were reported by experimental teams (Willson, 2014), whereas the PMOD composite uses a proxy model that is based on the linear regression of sunspot blocking and faculae brightening against satellite TSI observations (Fröhlich and Lean, 1998). To construct a TSI from a previous time period, two different approaches are employed: a reconstruction that is based on several different proxies for the solar irradiance (ACRIM-HS) or a statistical approach (PMOD). Proxies for the solar irradiance include the equatorial solar rotation rate, the sunspot structure, the decay rate of individual sunspots, the number of sunspots without umbra, the length and decay rate of the sunspot cycle, and the solar activity level.

Hoyt and Schatten (1993) constructed an irradiance model that was based on the solar cycle length, cycle decay rate, and mean level of solar activity for the period 1700–1874. From 1875–1992, a maximum of five solar indices were employed. The correlation between these indices and the phase coherence indicated that they have the same origin. Hoyt and Schatten (1993) interpreted this finding as a response to convection changes near the top of the convection zone in the Sun. All solar indices have maxima between 1920 and 1940; the majority of the maxima occur in the 1930s. The Hoyt-Schatten irradiance model has been calibrated and extended with the newest version of ACRIM TSI observations (e.g. Scafetta and Willson, 2014, Fig. 16); it is employed in this analysis. In the following section, this reconstruction is referred to as TSI-HS. A mostly rural Northern Hemisphere composite temperature series 1880–2013 shows strong correlation with the TSI-HS reconstruction, which indicates a strong solar influence on the temperature of the Northern Hemisphere (Soon et al., 2015).

The TSI-HS series covers the period from 1700–2013 A.D. To investigate longer periods to search for deep minimum periods, we have employed the statistical TSI index estimated by Velasco Herrera et al. (2015) from 1000 to 2100 A.D.. This index, which is referred to as TSI-LS, is estimated using the least squares support vector machine (LS-SVM) method, which is applied for the first time for this purpose. The method is nonlinear and nonparametric. The starting point is a probability density function (PDF) that was constructed from the PMOD or ACRIM composites. The function describes how many times a certain level of TSI has been observed. From this, normalized annual power anomalies are constructed. The TSI between 1610 and 1978 was determined by the LS-SVM method using the group sunspot number as an input after calibration between 1979 and 2013 with the ACRIM or PMOD composites. To estimate the TSI from 1000 to 1510 and from 2013 to 2100, the LS-SVM method and a nonlinear autoregressive exogenous model (NARX) were employed. In this study, we have employed the TSI reconstruction that was calibrated using the ACRIM TSI composite (Velasco Herrera et al., 2015).

1.3. Solar energy oscillation

An oscillating TSI variability is produced by forcing from an oscillating energy source. This oscillating energy source may be the solar inertial motion, processes in the interior of the Sun, solar tides and/or solar orbit oscillation around the solar system barycenter (SSB). The energy source for solar activity is the deceleration of the rotation of the Sun by magnetic field lines connected to interplanetary space. The solar wind carries mass away from the Sun; this magnetic braking causes a spin down of the solar rotation. Part of the decrease in rotational energy is the energy source for the solar dynamo, which converts kinetic energy into electromagnetic energy.

The classical interpretation of the solar dynamo is that it is placed in the transition zone between convection and radiation near the surface of the sun: the tachocline, located approximately 200,000 km below the surface. Strong electric currents originate from the interaction between the convection and the differential solar rotation. This leads to the formation of strong magnetic fields, which rise to the surface and exhibit various aspects of solar activity, such as spots, facular fields, flares, coronal mass emissions, coronal holes, polar bright points, and polar faculae, after having detached, as described by de Jager and Duhau (2011). They explain the 22-year Hale cycle attributed to magneto-hydrodynamic oscillations of the tachocline. This period is not constant. It persisted for approximately 23 years prior to the Maunder Minimum, during which it increased to 26 years. During the maximum of the last century, this period was as brief as 21 years. Gleissberg (1958); 1965) discovered a cycle of approximately 80 years in the amplitude of the sunspot numbers. This cycle is interpreted as the average of two frequency bands: one band from 50–80 years and one band from 90–140 years (Ogurtsov et al., 2002). An examination of the longest detailed cosmogenic isotope record (INTCAL98) of ^{14}C abundance, with a length of 12,000 years, reveals an average Gleissberg cycle period of 87.8 years. It is resolved in two combination periods of 91.5 ± 0.1 and 84.6 ± 0.1 yr (Peristykh and Damon, 2003). In addition to the variable Gleissberg period, a de Vries period from 170 to 260 years is observed in the ^{14}C and

^{38}Cl records. This period is fairly sharp with little or no variability (Ogurtsov et al., 2002).

Proxies that describe the magnetic fields in the equatorial and polar regions can describe the variability of the tachocline. A proxy for the equatorial (or toroidal) magnetic field is R_{max} (the maximum number of sunspots in two successive Schwabe cycles), and a proxy for the maximum poloidal magnetic field strength is aa_{min} (the minimum value of the measured terrestrial magnetic field difference). In a phase diagram based on theR_{max} and aa_{min} values, two Gleissberg cycles (1630–1724) and (1787–1880) were identified (Duhau and de Jager, 2008). The years 1630 and 1787 represent transition points, where phase transitions to the grand episodes (Maunder and Dalton minima) occurred. The lengths of the two Gleissberg cycles were 157 years and 93 years. The next Gleissberg cycle lasted 129 years until 2009, with an expected phase transition to a high state in 1924. Duhau and de Jager (2008) predicted that the transition in 2009 indicates a transition to a Maunder-type minimum that will start with cycle 25 in approximately 2020. Almost no existing models for the solar activity predicted the current weak cycle 24.

A principal component analysis of full disc magnetograms during solar cycles 21–23 revealed two magnetic waves that travel from opposite hemispheres with similar frequencies and increasing phase shifts (Shepherd et al., 2014; Zharkova et al., 2015). To understand this phase shift, they introduced a non-linear dynamo model in a two-layer medium with opposite meridional circulation. One dynamo is located in the surface layer, and the other dipole is located deep in the solar convection zone. The solar poloidal field is generated by these two dynamos in different cells with opposite meridional circulation. The observed poloidal-toroidal fields have similar periods of oscillation with opposite polarities that are in an anti-phase every 11 years, which explains the Schwabe period. The double-cell meridional circulation flow is detected with helioseismology by HMI/SDO observations (Zhao et al., 2013). Backward extrapolations of these two components revealed two 350-year grand cycles that were superimposed on a 22-year cycle. The beat between the two waves bears resemblance to the sunspot activity, including the Maunder and Dalton minima, and forecasts a deep minimum in this century. The low-frequency wave has a variable period length from 320 years (in the 18-20th centuries) to 400 years predicted for the next millennium.

Analysis of systematic variations of small-scale magnetic structures and EUV bright spots from the Solar and Heliospheric Observatory (SOHO) and Solar Dynamics Observatory (SDO) has led to a phenomenological model that explains the cyclic behavior of the sunspots as a systematic pattern of activity bands that are either stationary at high latitudes or move toward the equator in a 22-yr cycle (McIntosh et al., 2014a). The toroidal flux system that belongs to the 22-yr cycle is located deep in the convective interior at the bottom of the convection zone at $0.72r_s$ (McIntosh and Leamon, 2014b). In this model, the migration toward the equator is controlled by the solar (differential) rotation. The speed of migration toward the equator determines the solar activity. When the activity bands with opposite signs approach the equator, they cancel each other and a solar minimum is observed. If the approach is slow, a grand minimum may occur (McIntosh and Leamon, 2015). However, in this case, the 22 year cycle is still present in the polar regions, and a new band of activity begins every 22 years. This explains the variable length of solar cycles and why the cycle still is present even in the deep Maunder minimum, as observed in cosmogenic nucleids. The slow approach to a deep minimum may be the result of a random change in the length of a solar cycle. A long, weak cycle has a tendency to create another long and weak cycle, until finally being corrected by the high latitude 22-year clock, which then ends the deep minimum (McIntosh and Leamon, 2015). The deep minimum could also be a result of a systematic change in the rotation pattern, which may be caused by external forcing. This will be discussed in the following.

Another model is based on the observation that the thermal relaxation time in the convection zone is on the order of 10^5 years (Foukal et al., 2009), which is too long to explain the rapid decay of the magnetic field during a single solar cycle. A simple solution is to place the dynamo in small bubbles in the solar core, which change polarity every cycle due to interactions with the interplanetary magnetic field (Granpierre, 2015). The liberated rotational energy then forms buoyant hot bubbles that move toward the surface of the sun. These bubbles are observed on the surface of the sun as precursors for large flares. The largest flares have a high probability of appearing near the closest position of one or more of the tide-producing planets Mars, Venus, Earth and Jupiter (Hung, 2007; Mörner et al., 2015). The energy of the “hot bubbles” is increased by thermonuclear runaway processes in the bubbles, which appear at the surface of the sun as hot areas with a frozen magnetic field. In this process, planetary effects play an important role (Granpierre, 1990; 1996; Wolf and O’Donovan, 2007; Scafetta, 2012).

1.4. External forcing generated by the planets

Although the various dynamo models can explain the variations to some extent, few or no constraints on the periods exist. The majority of the explanations operate with a range of possible periods. The models do not explicitly determine whether the observed periods are random and stochastic or whether some period-forcing from external or internal sources occurs. In the following section, we investigate the external forcing that is generated by the planets in the solar system.

1.4.1. Solar inertial motion

Charvátová and Hejda (2014) have classified the solar inertial motion (SIM) in an ordered (trefoil) pattern with a length of approximately 50 years followed by disordered intervals. Exceptionally long (approximately 370 years) trefoil patterns appear with a 2402-year Hallstadt period. They determined that the deepest and longest solar activity minima (of Spörer and Maunder types) appeared in the second half of the 2402-year cycle, consistent with the most disordered type of SIM. The Dalton minimum appeared during a mildly disordered SIM (1787–1843), which repeats from 1985–2040. The solar orbit in the period 1940–2040, which is shown in Fig. 1, demonstrates this phase.

1.4.2. Interior of the sun as a rotating star

Wolf and Patrone (2010) have investigated how the interior of a rotating star can be perturbed when the star is accelerated by orbiting objects, as in the solar system. They present a simple model in which fluid elements of equal mass exchange positions. This exchange releases potential energy (PE) that is only available in the hemisphere that faces the barycenter of the planetary system, with a minor exception. This effect can increase the PE for a few well-positioned elements in the stellar interior by a factor of 7, which indicates that a star with planets will burn nuclear fuel more effectively and have a shorter lifetime than identical stars without planets. However, in the case of the Sun, occasional mass exchanges occur near the solar center, which activate a mixed shell situated at $0.16r_s$, where r_s is the solar radius. For this reason, the close passages of the barycenter are important because they can cause negative pulses in the PE. The energy liberated is a result of the roto-translational dynamics of the cell around the solar system barycenter. An analysis of the variation of the PE storage reveals that the maximum variations correspond to the documented grand minima of the last 1000 years because the PE minima are

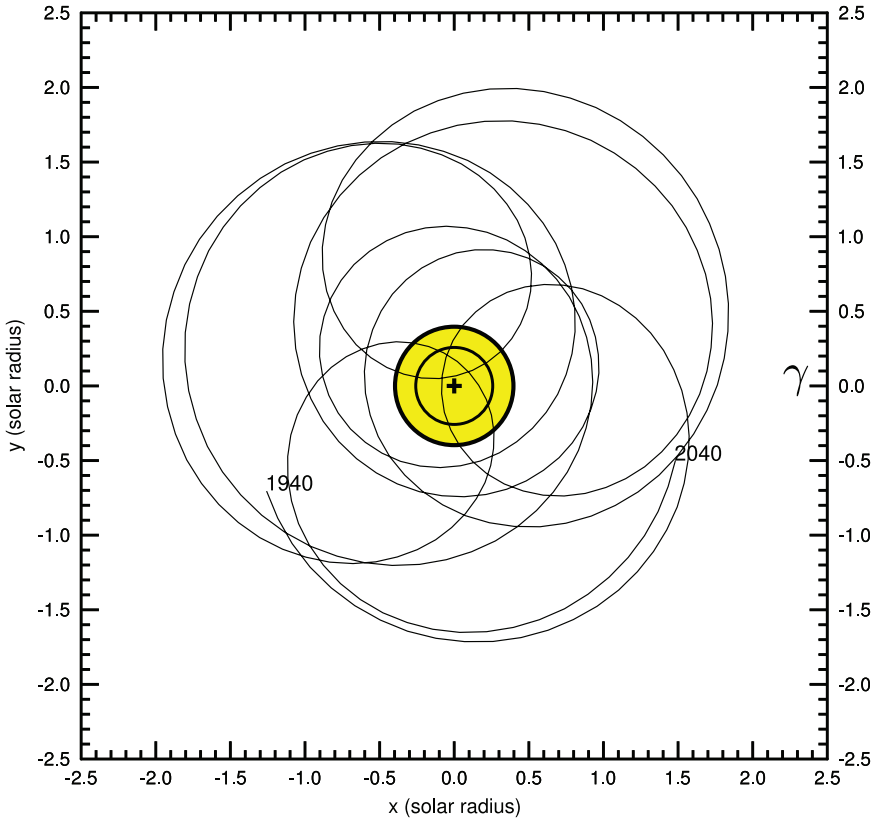

Fig. 1. Orbit of the solar center with respect to the solar system barycenter (SSB) (+) for the period 1940–2040 in the ecliptic plane defined in the direction of the Earth's vernal equinox (ϒ). The outer yellow circle represents the diameter of the Sun, and the inner circle with radius $0.65r_s$ represents a shell where the potential energy (PE) of the solar radiative zone can be affected if the solar center moves closer to the SSB (Cionco and Soon, 2015). (For interpretation of the references to colour in this figure legend, the reader is referred to the web version of this article.)

connected to periods in which the Sun moves close to the barycenter. Large reductions in the PE values occur when the giant planets are quasi-aligned, which occurred in approximately 1632, 1811 and 1990, separated by 179 years (Jose cycle). Because the planetary positions never exactly repeat, the PE variations exhibit a complex pattern that creates different minima (Cionco and Soon, 2015).

1.4.3. Solar inertial oscillations

The complex planetary synchronization structure of the solar system has been known since the time of Pythagoras of Samos (ca. 570-495 B.C.). Jose (1965) showed that the solar center moves in loops around the solar system barycenter (SSB). The average orbital period of 19.86 years corresponds to the heliocentric synodic period of Jupiter and Saturn. The modulation of the orbit by the outer planets Uranus and Neptune produces asymmetries in the orbital shape and period variations between 15.3 and 23.4 years (Fairbridge and Shirley, 1987). The solar motion differs from the Keplerian motion of planets and satellites in important ways. For instance, the velocity is occasionally highest when the distance from the Sun to the SSB is largest, and the solar angular momentum may vary by more than one order of magnitude over a period of ten years (Blizard, 1981). An analysis of solar orbits from 816–2054 A.D. covered seven complete Jose cycles of 179 years and indicated that prolonged minima can be identified by two parameters: the first parameter is the difference in axial symmetry of the orbit, and the second parameter is the change in angular momentum (torque) about the SSB. Based on these criteria, a new minimum should begin between 1990 and 2013 and end in 2091 (Fairbridge and Shirley, 1987).

The distance of the Sun from the barycenter, the velocity, and the angular momentum exhibit the same periodic behavior. The motion of the solar center around the SSB is typically prograde; however, in 1811 and 1990, the Sun occasionally passed near the SSB in a retrograde motion. Because the 1811 event occurred at the time of the Dalton minimum, a new minimum may occur in approximately 1990 (Cionco and Soon, 2015).

Scafetta (2014b) reviewed the investigations of the patterns that are described by the Sun and planets. He concluded that modern research shows that the planetary orbits can be approximated by a simple system of resonant frequencies and that the solar system oscillates with a specific set of gravitational frequencies, many of which range between three and 100 years, that can be constructed as harmonics of a base period of ~ 178.78 years.

1.4.4. Solar tidal oscillation

The tidal elongation at the surface of the Sun is on the order of 1–2 mm from the planets Venus and Jupiter and less from the other planets. Scafetta (2012) proposed that tidal forces, torques and jerk shocks act on and inside the Sun and that the continuous tidal massaging of the Sun should involve heating the core and periodically increasing the nuclear fusion rate. This action would amplify weak signals from the planets by a factor of $\sim 2 \times 10^6$. Even if the amplitude is small in the direction of a planet, it creates a wave that propagates with solar rotation and the velocity of the planet. If the planet has an elliptical orbit, then the variation in distance creates an additional modulation of the tidal wave that also effects the production of nuclear energy in the center of the Sun. Because more planets participate, this effect or GOs, will be a combination of phases and periods, which can be highly nonlinear.

Our hypothesis is that the solar position oscillation (SPO) represents an indicator of the tidal and inertial interaction between the giant planets Jupiter, Saturn, Neptune, Uranus and the Sun. The

SPO can be calculated from planetary Ephemeris as the movement of the Sun around the Solar System Barycenter (SSB). In Section 2, we describe the methods and data sets used to demonstrate a connection between SPO and TSI and SN variations. In Section 3, we present the results; in Section 4, we discuss the results and relate them to other investigations. We conclude in Section 5. Because the solar system and its planets have long lifetimes, we can expect forces in the same direction over long periods of time that may have a strong effect on long periods.

2. Materials and methods

2.1. Data

The objective of this study is to identify the source of possible stationary periods in TSI and SN variability. In this study, possible stationary periods are represented by first stationary periods, subharmonic periods and coincidence periods. First stationary periods have a period of T in the data series. Subharmonic periods have periods of $n*T$ for $n = 2, 3, 4\ldots$ Coincidence periods have a coincidence between two or more periods and may be represented by $n * T_1 = m * T_2$. Coincidence periods are stationary periods and introduce a new set of subharmonic periods. This study compares the identified stationary periods and period phase in two TSI data series, a sunspot data series and a SPO data series.

The SPO data series represents an indicator of the oscillating tidal and inertial interaction between the Sun and the large planets. The large planets have the following periods (in years): Jupiter $P(J, 11.862)$, Saturn $P(S, 29.447)$, Uranus $P(U, 84.02)$ and Neptune $P(N, 164.79)$. We analyze SPO data covering the period 1000 to 2100 A.D., where *SPOx* represents the *x*-direction of the *xyz*-vector and *SPOy* represents the *y*-direction. The source of the SPO data series is the JPL Horizon web interface (http://ssd.jpl.nasa.gov/horizons.cgi#top), which is based on the Revised July 31, 2013, ephemeris with the ICRF/J2000 reference frame, downloaded on 30.09.14 and later.

The total solar irradiance (TSI-HS) data series (e.g. Scafetta and Willson, 2014, Fig. 16) covers the period from 1700 to 2013 A.D. The source of the data series is Scafetta (personal communication. Dec. 2013). The total solar irradiance (TSI-LS) is based on the LS-SVM ACRIM data series (Velasco Herrera et al., 2015) and covers the period from 1000 to 2100 A.D. The source of the TSI-LS data series is Velasco Herrera (21.09.14. Personal communication). The sunspot data series is the group sunspot numbers from 1610 to 2015 A.D.. The source of the sunspot data series is SILSO (The World Data Center for the production, preservation and dissemination of the international sunspot number).

2.2. Methods

Possible stationary periods in the data series are identified in two steps. In the first step, a wavelet transform of the data series separates all periods into a wavelet spectrum. The autocorrelation of the wavelet spectrum then identifies dominant first stationary periods, subharmonic periods and the coincidence periods. Prior to the wavelet analysis, all data series are normalized by

$$x(t) = (y(t) - E[y(t)])/var(y(t)) \tag{1}$$

where $y(t)$ is the data series, $E[y(t)]$ is the mean value, $var(y(t))$ is the variance, and $x(t)$ is the scaled data series. The data series are scaled to compare the amplitudes from the oscillation periods and to reduce side effects in the wavelet analysis.

A wavelet transform of a data series $x(t)$ is capable of separating periods in the data series into a wavelet spectrum. The wavelet spectrum is computed by the transformation

$$W_{a,b}(t) = \frac{1}{\sqrt{a}} \int_R x(t)\psi\left(\frac{t-b}{a}\right)dt \tag{2}$$

where $x(t)$ is the analyzed time series; $\psi()$ is a coif3 wavelet impulse function (Daubechies, 1992; Matlab, 2015), which is chosen for its symmetrical performance and its ability to identify symmetrical periods in data series; $W_{a,\,b}(t)$ represents the computed wavelet spectrum; the parameter a represents a time-scaling parameter; and the parameter b represents a translation in time in the wavelet transformation. When $b = 0$ and $s = 1/a$, the wavelet spectrum $W(s, t)$ represents a set of moving correlations between $x(t)$ and the impulse function $\psi()$ over the entire time series $x(t)$. The relationship between the wavelet s and a sinus period T is approximately $T \sim 1.2s$ when using the coif3 wavelet function. In this investigation, the wavelet spectrum $W(s, t)$ has the spectrum range $s = 0, 1, 2\ldots 0.6N$, where N is the number of samples in the data series.

An autocorrelation transformation of the wavelet spectrum $W(s, t)$ identifies first periods, subharmonic periods and coincidence periods as maximum values in the computed set of autocorrelation functions. The set of autocorrelation functions is estimated by the transformation

$$R(s, m) = E[W(s, t)W(s, t + m)] \tag{3}$$

where $R(s, m)$ represents the correlations between samples, at a distance of m years, for a wavelet s in the wavelet spectrum $W(s, t)$.

3. Results

3.1. Sun position oscillation

The Sun moves in a closed orbit around the barycenter of the solar system. Fig. 1 shows the SPO in the ecliptical plane from 1940 to 2040. The solar system oscillation (SSO) is caused by the mutual gravity dynamics between the planet system oscillation (PSO) and the solar position oscillation (SPO). The solar position oscillation has oscillations in the (x, y, z) directions; they are represented by the data series *SPOx, SPOy* and *SPOz*. The movement appears rather chaotic, as shown in Fig. 1, because it mirrors the movements of the planets in their orbits. A first step in this investigation is to identify stationary periods and phase relations in the solar position between 1000 and 2100 A.D.

A wavelet spectrum represents a set of moving correlations between a data series and a scalable wavelet pulse. When the data series in the y-direction, namely, *SPOy*, is transformed to the wavelet spectrum $Wspoy(s, t)$, the spectrum represents a collection of dominant periods in the *SPOy* data series. A visual inspection of the wavelet spectrum $Wspoy(s, t)$ reveals a long-term dominant period of approximately $Pspoy(164)$ years. This period has a coincidence to the Neptune period P(N, 164.79). The data series *SPOx* and *SPOy* have identical periods; however, *SPOy* has a 90-degree phase delay with respect to *SPOx*.

The wavelet spectrum $Wspoy(s, t)$ is transformed to a set of autocorrelation functions $Rspoy(s, m)$, as shown in Fig. 2, in which each colored line represents a single autocorrelation function. The set of autocorrelations $Rspoy(s, t)$ shows the identified stationary periods in the wavelet spectrum $Wspoy(s, t)$. The first maximum represents the correlation to a first stationary period. Subharmonic periods have a maximum correlation at a distance (first period) $*n$, where $n = 1, 2, 3\ldots$. $Rspoy(s, m)$ identifies the following stationary periods: $P(spoy, 12)$ for $Rspoy(12) = 0.98$, $P(spoy, 29)$ for $Rspoy(29) = 0.95$, $P(spoy, 84)$ for $Rspoy(84) = 0.9$ and $P(spoy, 164)$ for $Rspoy(164) = 0.9$. The same periods are associated with the

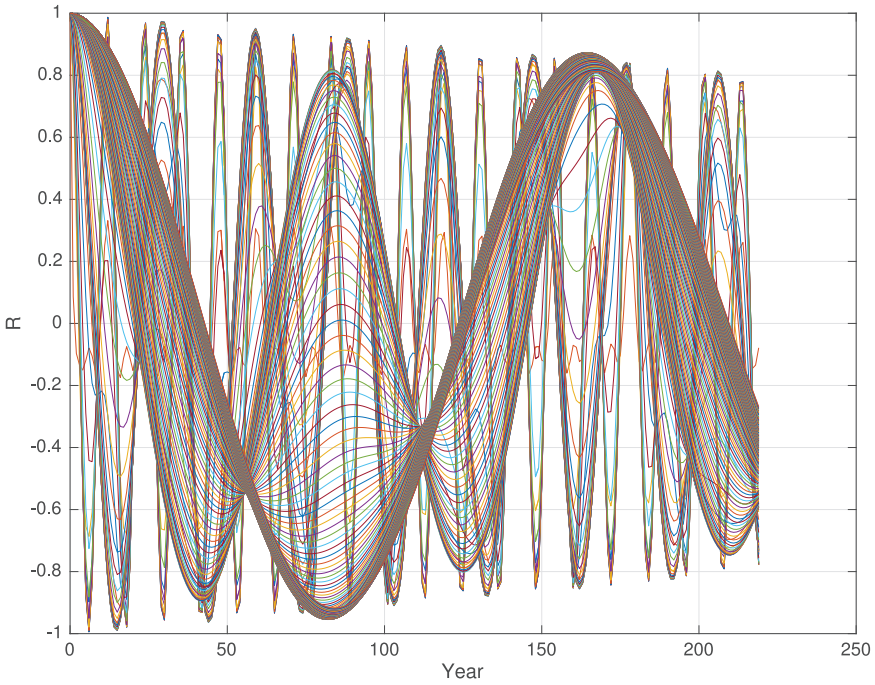

Fig. 2. Autocorrelations *Rspoy*(*s, m*) of solar position oscillation (*SPOy*) wavelet spectrum *Wspoy*(*s, t*) for $m = 0 \ldots 225$. Each colored line represents a single autocorrelation function.

PSO periods *P*(*J*, 11.862), *P*(*S*, 29.447), *P*(*U*, 84.02) and *P*(*N*, 164.79), which indicates that the planets Jupiter, Saturn, Uranus and Neptune in the planetary system are controlling the SPO.

A coincidence between subharmonic periods will amplify the coincidence period and introduce a new set of stationary periods. The autocorrelation spectrum *Rspoy*(*s, m*) in Fig. 2 shows a set of subharmonic periods, namely, *P*(*spoy, n*∗12), *P*(*spoy, n*∗29) and *P*(*spoy, n*∗84), where $n = 1, 2, 3 \ldots$. The identified coincidence periods have mean values of $(P(spoy, 5 * 12) + P(spoy, 2 * 29))/2 = P(spox, 59)$ for $RW(spoy, 59) = 0.95$, $P(spoy, 7 * 12) + P(spoy, 3 * 29) + P(spoy, 84))/3 = P(spoy, 85)$ for $RW(spoy, 85) = 0.9$, $(P(spoy, 10 * 12) + P(spoy, 4 * 29))/2 = P(spoy, 118)$ for $Rspoy(118) = 0.9$ and $(P(spoy, 2 * 84) + P(spoy, 164))/2 = P(spoy, 166)$ for $Rspoy(166) = 0.9$. Fig. 2 reveals that the majority of the SPO periods are mutually related by resonance. The new modulated periods are *P*(*spoy*, 59) and *P*(*spoy*, 118).

The stationary long wavelet periods *Wspoy*(84, *t*) and *Wspoy*(164, *t*) have maxima in approximately 1820, and *Wspoy*(29, *t*) has a maximum in approximately 1812. The identified stationary periods may be transformed to the following model:

$$P(spoyc, 29, t) = RW(spoy, 29)\cos(2\pi(t - 1812))/29.447) \quad (4)$$

$$P(spoyc, 84, t) = RW(spoy, 85)\cos(2\pi(t - 1820))/84.02) \quad (5)$$

$$P(spoyc, 164, t) = RW(spoy, 164)\cos(2\pi(t - 1820))/164.97) \quad (6)$$

Using this model, the year 1820 may serve as a phase reference for the *SPOy* periods, TSI variability and solar variability (SN). The data series *SPOx* has the same stationary periods but a different phase. *P*(*spoxc*, 84, *t*) has a maximum at approximately 1797, which represents a phase shift of approximately $\pi/2$. *P*(*spoxc*, 164, *t*) has a maximum at approximately 1779. The maxima in *SPOy* and *SPOx* correspond to the minima in *SPOÿ* and *SPOẍ*. The deterministic model Eqs. 4–(6) has the sum $P(spoyc, 29, t) + P(spoyc, 84, t) + P(spoyc, 164, t)$ and a maximum in approximately 1812.

3.2. TSI-HS variability

The total solar irradiance (TSI) represents the measured irradiation Wm^{-2} at the average distance from the Sun to the Earth. Fig. 3 shows an annual mean total solar irradiance (TSI-HS) data series (Scafetta and Willson, 2014) that covers the period from 1700 to 2013 A.D. A simple visual inspection of this data series reveals some variability properties. The TSI-HS data series has fluctuations of approximately 3–4 Wm^{-2}. The TSI fluctuations have minima in approximately 1700 (or before), 1800, 1890, and 1960, with gaps of approximately 100, 90, and 70 years, or a mean minimum period of approximately 86 years. The TSI-HS data series has maxima in 1770, 1830, and 1950, with gaps of approximately 60 and 120 years. The mean maximum fluctuation period in the TSI-HS data series is approximately 75 years, or 11 years less than the mean minimum period. Transformation of the TSI data series into a wavelet spectrum may separate dominant periods.

The transformed wavelet spectrum *Whs*(*s, t*) represents a set of separated wavelet periods from the TSI-HS data series. Fig. 4 shows the computed wavelet spectrum of the TSI-HS data series from 1700 to 2013. In this figure, the wavelet scaling range is $s = 1 \ldots 0.6N$, and the data series contains $N = 313$ data points. A visual inspection of the TSI wavelet spectrum reveals the dominant periods in the TSI data series in the time window between 1700 and 2013. The long wavelet period has a maximum in 1760, 1840, 1930, and 2000, with a mean gap of approximately 80 years.

The autocorrelation spectrum *Rhs*(*s, m*) of the wavelet spectrum *Whs*(*s, t*) identifies stationary periods in the wavelet spectrum. The maximum values in the autocorrelation spectrum *Rhs*(*s, m*) represent a correlation to stationary periods in the TSI-HS wavelet spectrum. Fig. 5 shows the autocorrelation spectrum *Rhs*(*s, m*) of the wavelet spectrum *Whs*(*s, t*) of the TSI-HS data series.

Analysis of the autocorrelation spectrum *Rhs*(*s, m*) reveals a set of stationary periods in the *Whs*(*s, t*) wavelet spectrum. The identified first cause stationary periods comprise the period set *P*(*hs*, 11) for $Rhs(11) = 0.55$, $P(hs, 49)$ for $Rhs(49) = 0.55$, $P(hs, 86)$ for $Rhs(86) = 0.65$ and *P*(*hs*, 164) for $RWhs(164) = 0.7$. The identified

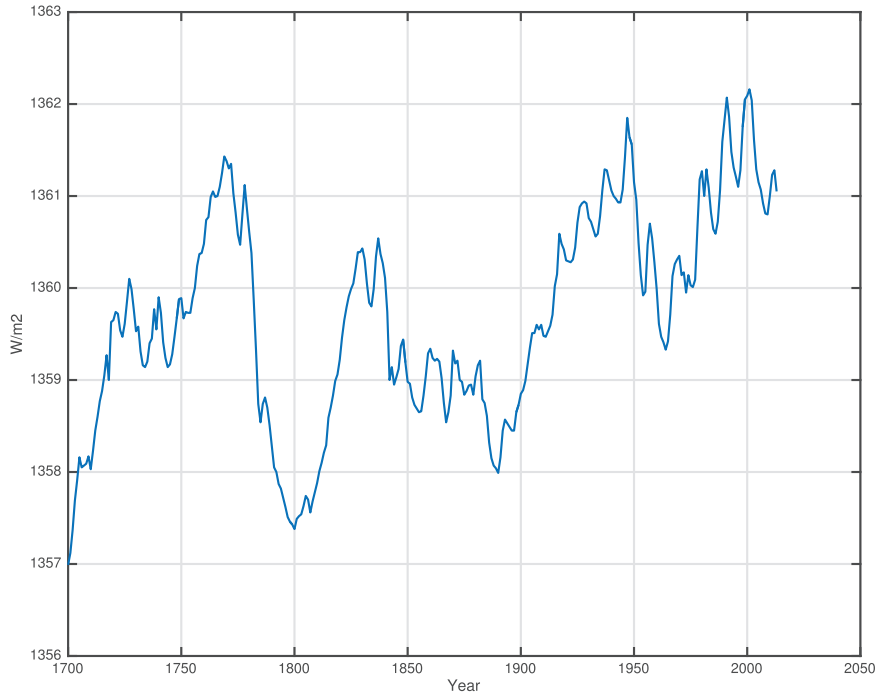

Fig. 3. TSI-HS total solar irradiance from 1700 to 2013 A.D. (Scafetta and Willson, 2014).

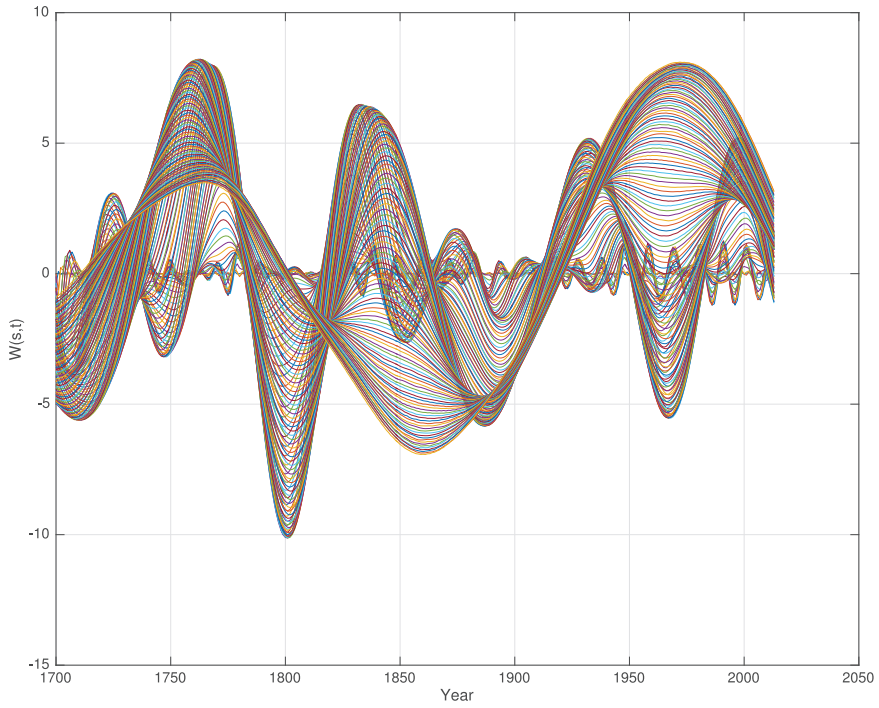

Fig. 4. Wavelet spectrum $Whs(s, t)$ of the TSI-HS data series for $s = 1 \ldots 190$.

stationary periods are associated with the PSO periods $P(J, 11.862)$, $P(S, 29.447)$, $P(U, 84.02)$ and $P(N, 164.79)$. The identified stationary period $P(hs, 49)$ may be explained by possible modulation between Saturn and Neptune periods: $2/(1/P(S, 29.447) + 1/P(N, 164.79)) = P(S, N, 49.96)$. This finding indicates that the TSI-HS variability is related to the solar position oscillation, which is controlled by the periods of the large planets Jupiter, Saturn, Uranus and Neptune. Additional analysis indicates that the dominant wavelet periods $Whs(11, t)$ and $Whs(49, t)$ are mean estimates. $Whs(11, t)$ has phase disturbance, and $Whs(49, t)$ has a phase reversal, as shown in Fig. 6. They do not have stable phases and represent mean periods.

Fig. 6 presents the identified dominant stationary wavelet periods $Whs(49, t)$, $Whs(86, t)$ and $Whs(165, t)$ from the autocorrelation functions in $Rhs(s, m)$. This figure shows that the wavelet period $P(hs, 49)$ has a time-variant phase and is not a stable period. The TSI-HS wavelet periods $Whs(49, t)$ and $Whs(86, t)$ have a negative value coincidence in the period from 1786 to 1820. $Wspoy(84, t)$ has an estimated maximum velocity and $Wspox(84, t)$ has a maximum state at approximately 1797. The dominant wavelet period

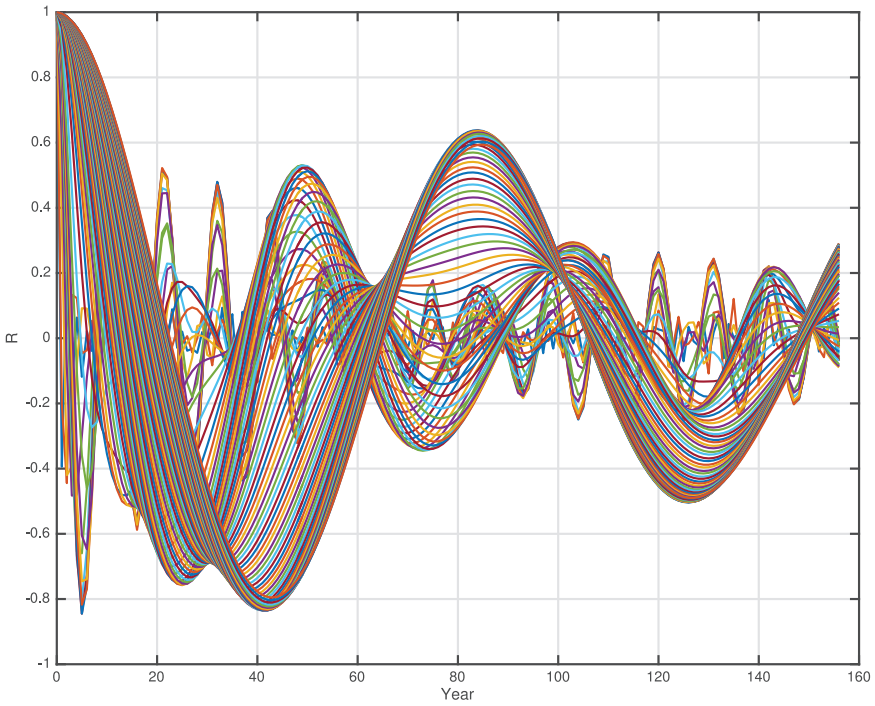

Fig. 5. Autocorrelations *Rhs*(*s*, *m*) of the TSI-HS wavelet spectrum *Whs*(*s*, *t*) for $s = 1 \dots 190$ and $m = 1 \dots 160$.

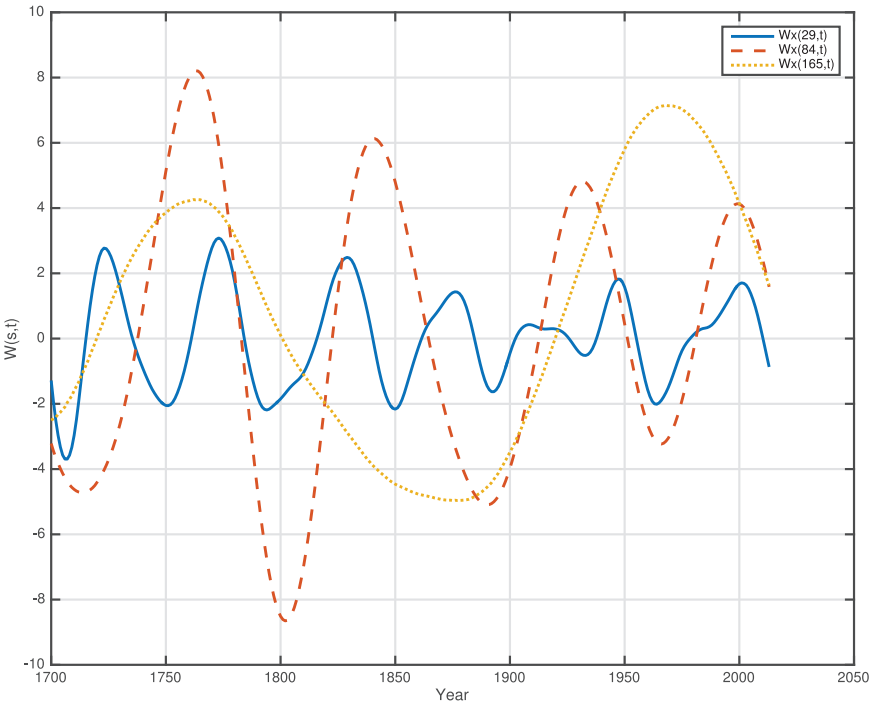

Fig. 6. The identified stationary wavelet periods *Whs*(49, *t*), *Whs*(86, *t*) and *Whs*(165, *t*) from the TSI-HS wavelet spectrum *Whs*(*s*, *t*).

Whs(84, *t*) has a minimum state at approximately 1803, or a phase delay of approximately 0.15π (rad/yr) between the *Wspox*(84, *t*) maximum and the minimum *Whs*(84, *t*). Uranus was in perihelion in 1798. This indicates a relation between the minimum Uranus distance to the Sun and a minimum in TSI-HS around 1800.

The correlation between the TSI-HS data series and the identified dominant wavelet periods $Whs(49,t) + Whs(86,t) + Whs(164,t)$ is estimated to be $R = 0.93, Q = 46.6$ (Pearson correlation coefficient) in $N = 312$ samples. The correlation $R = 0.93$ reveals a close relation between the TSI-HS variability and the solar position oscillation, which is controlled by Jupiter, Saturn, Uranus and Neptune.

3.2.1. Deterministic model for TSI-HS variability

The identified stationary periods *Whs*(86, *t*) and *Whs*(164, *t*) may be represented by a deterministic model from the sum of the stationary cosine functions:

$$P(hsc, 84, t) = -Rhs(86)\cos(2\pi(t - 1803)/84.02) \quad (7)$$

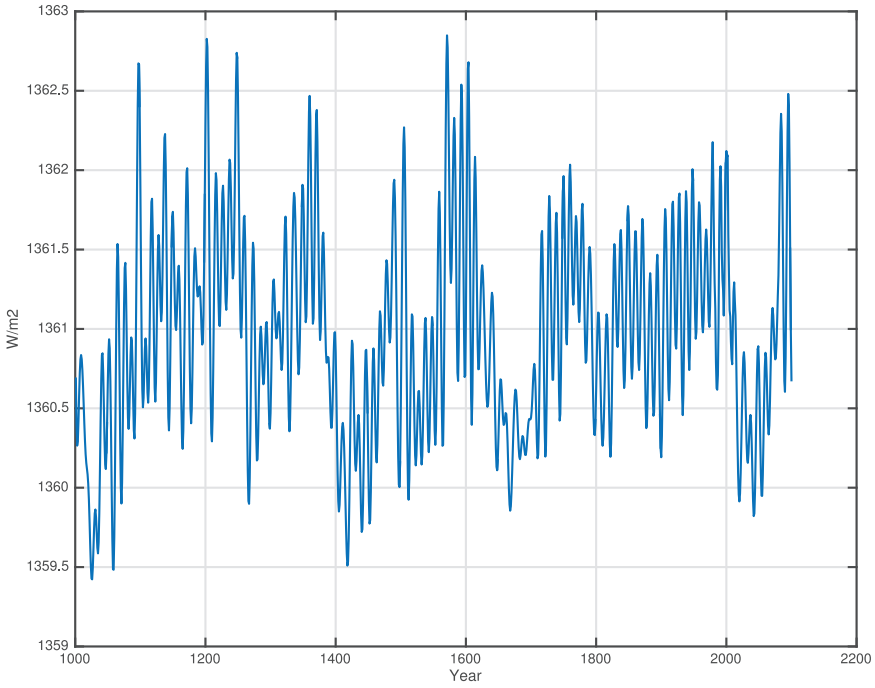

Fig. 7. TSI-LS data series from 1000 to 2100 A.D. Velasco Herrera et al. (2015).

$$P(hsc, 164, t) = -Rhs(164)\cos(2\pi(t - 1860)/164.97) \quad (8)$$

$$P(hsc, t) = P(hsc, 84, t) + P(hsc, 164, t) \quad (9)$$

where $R(hs, 86)$ and $R(hs, 164)$ represent estimated correlations in the autocorrelation. The phase relation between the maximum value of $Pspox(84, t)$ in 1797 and the minimum value $P(hsc, 84, t)$ in 1803 is approximately 0.15π (rad/year). The year 1797 is also the year where Uranus was in perihelion. Moreover, note that the minimum value of $P(hs, 164, t)$ (Eq. 8) is close to the time of Neptune in perihelion. This indicates a delayed response from the SPO periods on the TSI-HS variability. The correlation between the 84-year wavelet periods $P(hsc, 84, t)$ and $W(hsc, 84, t)$ is estimated to be $Rhs, hsc(84) = 0.83$. The correlation between the 164-year periods is $Rhs, hsc(164) = 0.88$. The correlation between the TSI-HS data series and the sum $P(hsc, t)$ is estimated to be $R = 0.55$. These results indicate that the dominant wavelet periods $Whs(84, t)$ and $Whs(164, t)$ have stable phases from 1700 to 2013 A.D.

From the deterministic model (Eq. 9) of the TSI-HS data series, we estimate grand minimum periods when $P(hsc, t) \leq -1$. These minima, which are compared with named solar minima, are shown in Table 2. The next deep minimum is estimated to occur in approximately 2050. The TSH-HS data series can estimate time periods up to a maximum of (2013-1700)/2=156 years and supports reasonably good estimates of periods of approximately one hundred years. Longer time period estimates require longer data series.

3.3. TSI-LS variability

The TSI-LS data series (Fig. 7) covers a period of 1100 years from 1000 to 2100 A.D., where the time period from the present to 2100 is forecasted. A realistic hundred-year forecast or hindcast has to be based on possible deterministic periods in the data series. A coherence analysis of the wavelet spectra $Whs(s, t)$ and $Wls(s, t)$ shows a coherency $Chs, ls = 0.8 - 0.95$ for periods between 48 years and 86 years, which indicates that the TSI-HS data series and the TSI-LS data series have the same periods of 48–86 years from 1700 to 2013 A.D.

The TSI-LS data series is analyzed by computing the wavelet spectrum $Wls(s, t)$ and the autocorrelation spectrum $Rls(s, m)$, and the latter is shown in Fig. 8. The identified stationary periods in the autocorrelation spectrum $Rls(s, m)$ are $P(ls, 11)$ for $Rls(11) = 0.8$, $P(ls, 18)$ for $Rls(18) = 0.3$, $P(ls, 29)$ for $Rls(29) = 0.2$, $P(ls, 83)$ for $Rls(83) = 0.17$, $P(ls, 125)$ for $Rls(125) = 0.6$, $P(ls, 210)$ for $Rls(210) = 0.35$ and $P(ls, 373)$ for $Rls(373) = 0.5$; the last is not shown in Fig. 8. These periods are associated with the identified stationary periods in the TSI-HS data series, the SPO data series periods and the PSO periods $P(J, 11.862)$, $P(S, 29.447)$ and $P(U, 84.02)$. The difference is the smaller correlation value in the autocorrelation $Rls(s, m)$. The smaller correlation values may be explained by phase errors in this long data series.

The autocorrelation spectrum $Rls(s, m)$ (Fig. 8) shows coincidence periods between $P(ls, 3 * 11) = P(ls, 33)$ and $P(ls, 2 * 18) = P(ls, 36)$, between $P(ls, 5 * 11) = P(ls, 55)$ and $P(ls, 3 * 18) = P(ls, 54)$, and between $P(ls, 8 * 11) = P(ls, 88)$ and the first period $P(ls, 83)$. The coincidence period $P(ls, 55)$ introduces the subharmonic periods $P(ls, n{*}55)$ for $n = 1, 2, 3 \ldots$. The new information in $Rls(s, m)$ is an identification of the dominant first cause periods $P(ls, 18)$, $P(ls, 125)$ and $P(ls, 210)$. These periods have a combination resonance that is created by a 2/3 resonance and a 5/2 resonance. The stationary periods have a perfect relation to the Jupiter and Uranus periods when $P(ls, 18) = P(ls, 3 * 11/2)$ is related to $P(ls, 3 * 11.862/2 = 17.793)$, $P(ls, 126) = P(ls, 3 * 84/2)$ is related to $P(ls, 3 * 84.02/2 = 126.03)$ and $P(ls, 210) = P(ls, 5 * 84/2)$ is related to the period $P(ls, 5 * 84.02/2 = 210.05)$. The period $P(ls, 125)$ introduces a set of subharmonic periods $P(ls, n{*}125)$, where $n = 1, 2, 3 \ldots$. In this investigation, we have only selected the third subharmonic period $P(ls, 3 * 126.03 = 378.09)$, which is the most dominant.

The autocorrelation spectrum $Rls(s, m)$ shows that the period $Wls(125, t)$ represents the dominant stationary amplitude variability in the TSI-LS data series. Fig. 9 shows the identified long-term stationary periods $Wls(124, t)$, $Wls(210, t)$, and $Wls(373, t)$ and the mean amplitude variation for these periods. The correla-

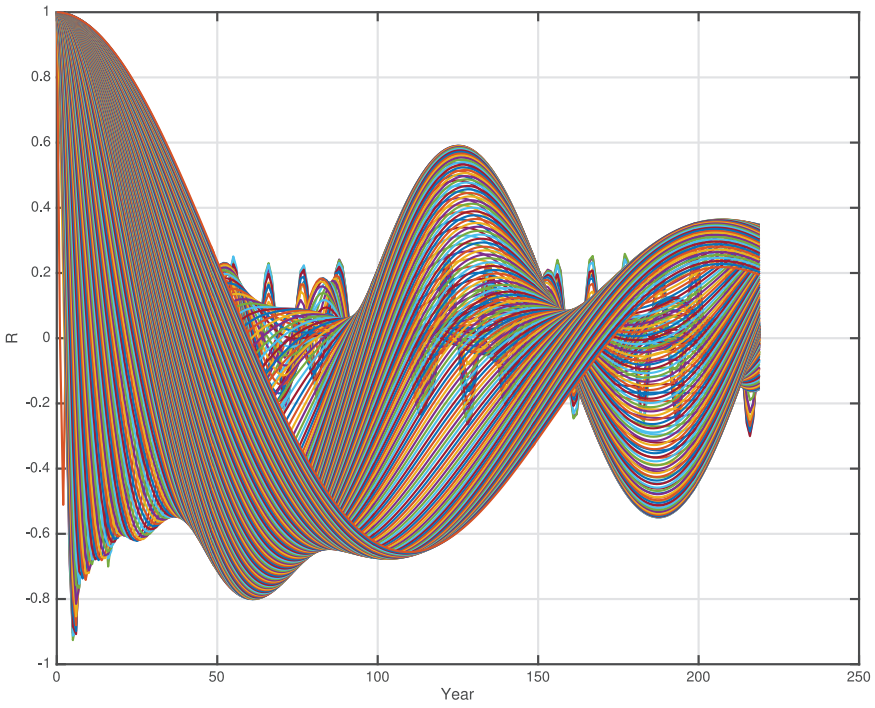

Fig. 8. Autocorrelations *Rls*(*s*, *m*) of the TSI-LS wavelet spectrum *Wls*(*s*, *t*) for $s = 0 \ldots 600$ and $m = 0 \ldots 225$.

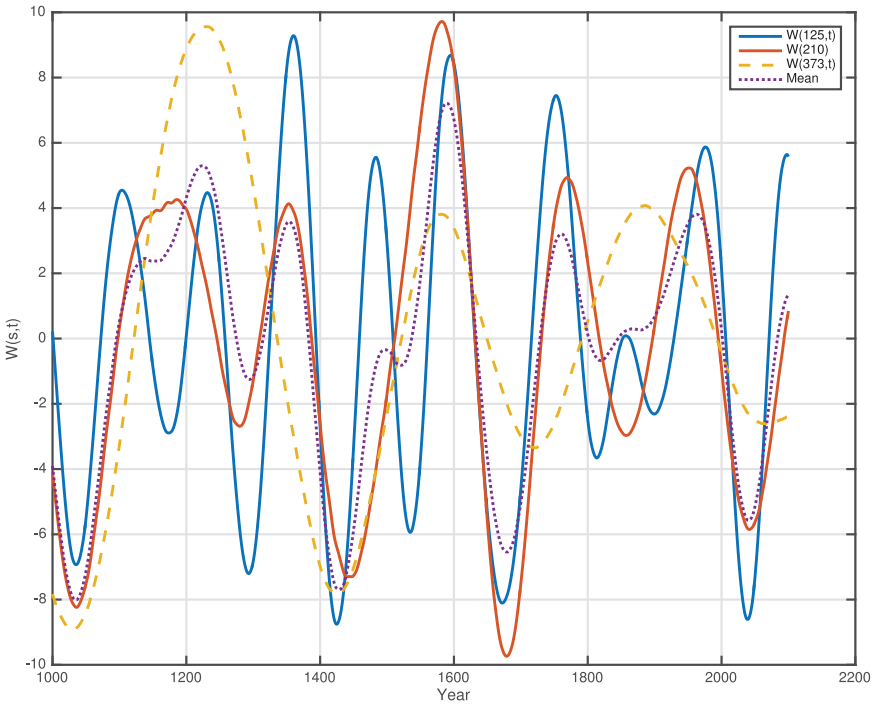

Fig. 9. Identified long stationary wavelet periods *Wls*(125, *t*), *Wls*(210, *t*)*Wls*(373, *t*) and their mean value.

tion between TSI-LS and the mean is estimated to be $R = 0.7$ for N=1100 samples and the quality Q=27.4. The mean of the identified wavelets *Wls*(125, *t*), *Wls*(210, *t*), *Wls*(373, *t*) has a negative state in the periods (1000–1100), (1275–1314), (1383–1527), (1634–1729), (1802–1846) and (2002–2083). The mean has a minimum state in the years 1050, 1293, 1428, 1679, 1820, and 2040.

3.3.1. Deterministic model for TSI-LS variability

The identified stationary dominant periods *Wls*(125, *t*), *Wls*(210, *t*), and *Wls*(373, *t*) may be represented by the deterministic stationary model from the sum of the cosine functions

$$P(lsc, 126, t) = Rls(125)\cos(2\pi\,(t - 1857)/(3 * 84.02/2)) \quad (10)$$

$$P(lsc, 210, t) = Rls(210)\cos(2\pi\,(t - 1769)/(5 * 84.02/2)) \quad (11)$$

$$P(lsc, 378, t) = Rls(373)\cos(2\pi\,(t - 1580)/(9 * 84.02/2)) \quad (12)$$

$$P(lsc, t) = P(lsc, 126, t) + P(lsc, 210, t) + P(lsc, 378, t) \quad (13)$$

where *Rls*(125), *Rls*(210) and *RWls*(373) represent the maximum period correlations in the autocorrelation *Rls*(*s, m*). The correlation between the 125-year wavelet period *W*(*ls*, 125, *t*) and the stationary period *P*(*lsc*, 126, *t*) is estimated to be $Rls, lsc(125) = 0.9$ for N=1040 samples and Q = 53.7, $Rls, lsc(210) = 0.67$ for N=1000 and Q = 28.9, and $Rls, lsc(378) = 0.68$ for N = 1000 and Q = 28.8. The period *Plsc*(375, *t*) has the correlation $Rls, lsc(378) = 0.67$ to the identified wavelet period *Wls*(373, *t*) for N = 1000 samples and Q = 28.13. The dominant wavelet periods *Wls*(125, *t*) and *Wls*(375, *t*) have a stationary period and an approximately stable phase in the period from 1000 to 2100 A.D. A correlation of long data series is sensitive to phase noise. The sum of the stationary periods *P*(*lsc, t*) represents a mean TSI-LS variability. The correlation to the TSI-LS data series is estimated to be $Rlsc, ls(126 + 210 + 378) = 0.55$ for N=1100 and Q=21.5. This analysis indicates that the TSI-LS variability has been influenced by stationary periods that are controlled by the Uranus period *P*(*U*, 84.02). A minimum of *P*(*lsc*, 126, *t*) is in 1794, which is close to the time of Uranus's perihelion position, whereas *P*(*lsc*, 210, *t*) has a minimum in 1874, which is 0.7π (rad/yr) after the *Pspox*(*max*). This result indicates that the phases of these periods are synchronized with Uranus's perihelion position in 1798.

The deterministic model (Eq. 13) of the TSI-LS data series may represent an index of minimum irradiation periods, as shown in Table 2. With this index, the chosen data series references a TSI minimum when the state is $P(lsc, t) \le -0.5$, a Dalton-type minimum when $P(lsc, t) \le -0.7$ and a grand minimum when $P(lsc, t) \le -1.0$. The identified minima from this model are $P(lsc, t) \le -1.0$ for the time period (1014–1056); $P(lsc, t) \le -0.5$) for (1276–1301); $P(lsc, t) \le -1.0$ for (1404–1435), which has a minimum of -1.215 in the year 1419; $P(lsc, t) \le -0.5$ for (1662–1695), which has a minimum of -0.91 in the year 1672; and $P(lsc, t) \le -0.5$ for (1775–1819), which has a minimum of -0.81 in the year 1796. The computed subsequent minimum time period is $P(lsc, t) \le -0.5$ for (2035–2079), which has a minimum of -0.79 in the year 2057. In this model, a Dalton-type minimum has a minimum state at approximately -0.7. The Maunder minimum is between -0.7 and -1.0, as shown in Table 2. The computed minimum of -0.79 in the year 2057 indicates an expected Dalton-Maunder-type minimum. Deterministic periods from the TSI-LS model have a state $P(lsc, t) \ge +0.5$ index for the periods (1093–1134), (1198–1241) and (1351–1357); $P(lsc, t) \ge +1.0$ index for the period (1582–1610); $P(lsc, t) \ge +0.5$ for (1945–2013); and $P(lsc, t) \ge +1.0$ for (1959–2001), which has a maximum of 1.4 in 1981.

3.4. Sunspot variability

The sunspot data series *SN*(*t*) is an indicator of the solar variability. Fig. 10 shows the group sunspot number data series that covers a period of approximately 400 years from 1610 to 2015 A.D. From this 400-year data series, we can estimate periods of up to approximately 200 years. Periods with few sunspots are associated with low solar activity and cold climate periods. Periods with many sunspots are associated with high solar activity and warm climate periods. If a relation exists between solar periods and climate periods, then we may expect a relation between the periods in the TSI variability and solar variability.

Fig. 11 shows the computed wavelet spectrum *Wsn*(*s, t*) of the *SN*(*t*) data series from 1610 to 2015, with the wavelet scaling parameter $s = 1 \ldots 6N$. A visual inspection of the wavelet spectrum shows a maximum at the approximate years (1750, 1860, and 1970), which represents periods of approximately 110 years. The time from 1750 to 1970 represents a period of 220 years. Temporary periods of approximately 50 years from approximately 1725 and 1930 may be confirmed by computing the autocorrelation wavelet spectrum *Rsn*(*s, t*).

The computed set of autocorrelations *Rsn*(*s, m*) of the wavelet spectrum *Wsn*(*s, t*) is shown in Fig. 12. The wavelet spectrum *W*(*sn, t*) has the stationary periods *P*(*sn*, 11) for $Rsn(11) = 0.73$, *P*(*sn*, 22) for $Rsn(22) = 0.35$ and *P*(*sn*, 86) for $Rsn(86) = 0.35$. The identified period *P*(*sn*, 11) represents the Schwabe cycle and corresponds to the TSI periods *P*(*hsi*, 11) and *P*(*ls*, 11), the SPO period *P*(*spox*, 11), and the Jupiter period *P*(*J*, 11.862).

The period *P*(*sn*, 11) introduces the subharmonic period $P(sn, 5 * 11) = P(sn, 55)$ for $Rsn(55) = 0.43$, which introduces the subharmonic periods *P*(*sn*, 110) for $Rsn(110) = 0.40$ and *P*(*sn*, 210) for $Rsn(210) = 0.36$. The period *P*(*sn*, 55) is a temporary stationary period from 1610 only when *P*(*sn*, 110) has a positive state. An inspection of *P*(*sn*, 55) reveals that the period is stationary when *P*(*sn*, 210) has a positive state from 1726–1831 and from 1935. The period *P*(*sn*, 55) shifted to *P*(*sn*, 2∗55) when *P*(*sn*, 210) has a negative state from 1831–1935. A possible explanation is a 5/2 relation between the periods *P*(*U*, 84.04) and *P*(*sn*, 210) (Eq. 16).

Fig. 12 shows that the period *P*(*sn*, 55) has combination resonance periods with a 3/2 relation $P(sn, 3 * 55/2 = 84)$ to the Uranus period *P*(*U*, 84.02). The 3/2 correlation to the *P*(*ls*, 84) period and the Uranus period *P*(*U*, 84.02) explains the synchronization between the SN variability and the TSI-LS variability. The dominant period *P*(*sn*, 110) is a coincidence period in the subharmonic period $P(sn, 2 * 55 = 110)$, which has a combination resonance to the Neptune period by $P(sn, 2 * 164, 79/3 = 109, 86)$. The identified long stationary period *P*(*sn*, 210) is related to a 5/2 combination resonance to Uranus by $P(U, 5 * 84.02/2 = 210.05)$. The period *P*(*sn*, 210) corresponds to the TSI-LS period *P*(*ls*, 210). The identified periods have a subharmonic resonance in the Jupiter period *P*(*J*, 11.862). The correlation between the data series SN(t) and the dominant wavelet periods $W(sn, 55, t) + W(sn, 110, t) + W(sn, 210, t)$ is estimated to be $R = 0.51$ for N=404 and Q=11.8.

3.4.1. Deterministic model of SN variability

The identified temporary stationary periods *Wsn*(55, *t*), *Wsn*(110, *t*) and *Wls*(210, *t*) may be represented by the following deterministic model

$$P(snc, 56, t) = Rsn(55)\cos(2\pi\,(t - 1782)/(2 * 84.02/3)) \quad (14)$$

$$P(snc, 112, t) = Rsn(110)\cos(2\pi\,(t - 1751)/(4 * 84.02/3)) \quad (15)$$

$$P(snc, 210, t) = Rsn(210)\cos(2\pi\,(t - 1770)/(5 * 84.02/2)) \quad (16)$$

$$P(snc, t) = P(snc, 56, t) + P(snc, 112, t) + P(snc, 210, t) \quad (17)$$

where *Rsn*(55), *Rsn*(110) and *Rsn*(210) represent the maximum correlation in the autocorrelation *Rsn*(*s, m*). This model is, however, a simplified model. Fig. 11 shows that the *Rsn*(55) amplitude is controlled by the *Rsn*(110) amplitude, which indicates that the period *P*(*sn*, 55) is temporarily stable. The correlation between the 55-year wavelet periods *W*(*sn*, 55, *t*) and the stationary period *P*(*snc*, 55, *t*) is estimated to be $Rsn, snc(55) = 0.66$ for N = 354 samples and Q =16.6. The correlations are $Rsn, snc(110) = 0.9$ for N = 304 and Q = 36 and $Rsn, snc(210) = 0.9$ for N=304 and Q=36. The correlation between the sum $W(sn, 55, t) + W(sn, 110, t) + W(sn, 210, t)$ and the deterministic model from (Eq. 17) is estimated to be $R = 0.84$ for N = 304 and Q = 29.8. Minimum states that correspond to negative values of the stationary model correspond to the observed minima, as shown in Table 2. The model indicates a future minimum in the period 2018–2055 with an extreme value in 2035.

This analysis indicates that the sunspot variations are controlled by the Uranus period *P*(*U*, 84.02), which introduces a 2/3 resonance to the period *P*(*sn*, 55, *t*) and a 5/2 resonance to the period *P*(*sn*, 210). The TSI-LS data series and the sunspot data series have stationary coincidence periods with *P*(*ls*, 11) and *P*(*sn*, 11), with *P*(*ls*,

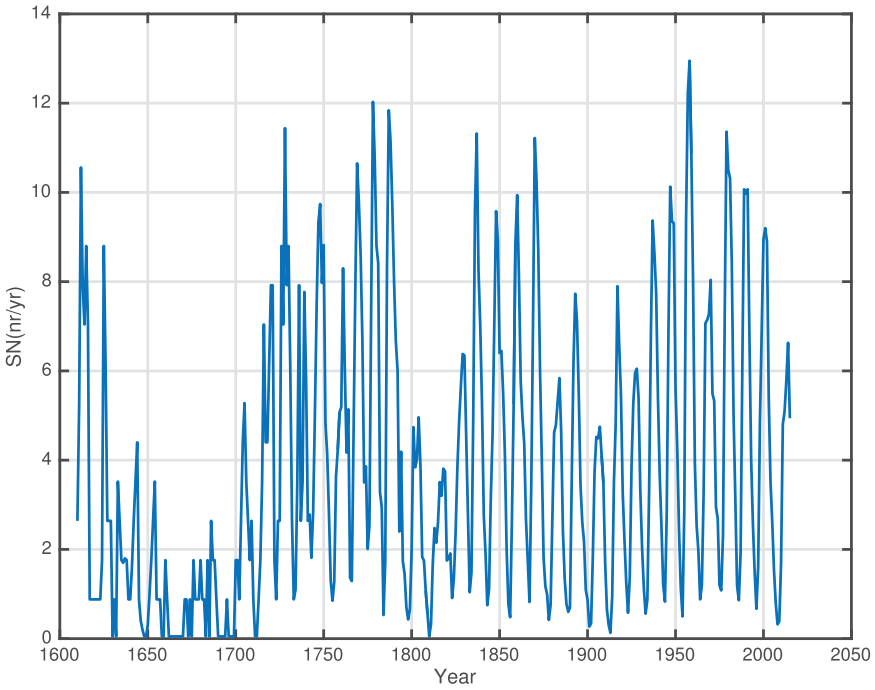

Fig. 10. Solar variability represented by the yearly average group sunspot number series $SN(t)$, estimated from 1610 to 2015 A.D. (SILSO data/image, Royal Observatory of Belgium, Brussels).

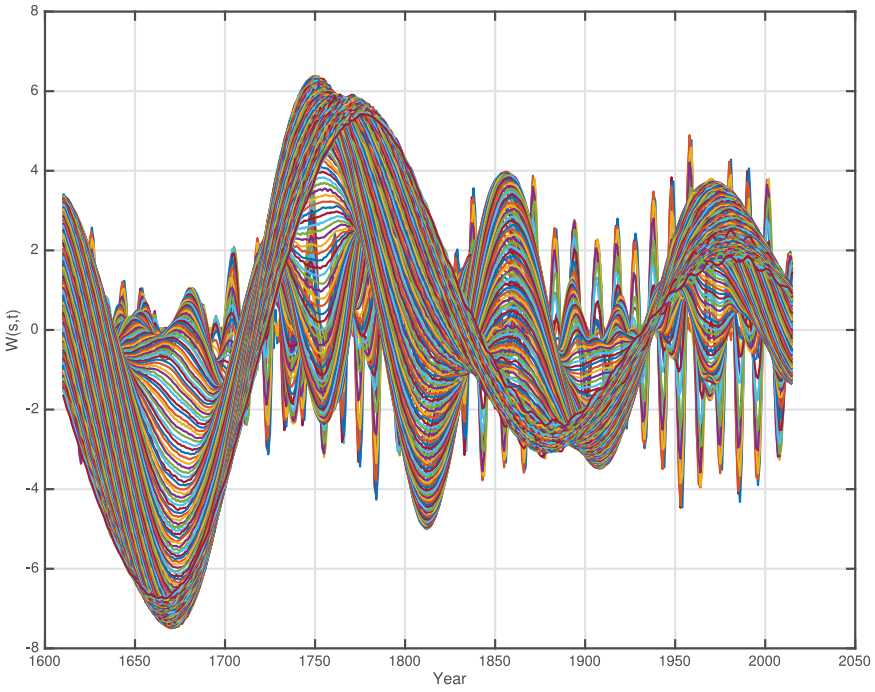

Fig. 11. Wavelet spectrum $Wsn(s, t)$ of the sunspot data series $SN(t)$.

125) and $P(sn, 110)$ and with $P(ls, 210)$ and $P(sn, 210)$. The difference between the stationary periods $P(ls, 125)$ and $P(sn, 110)$ indicates a limited direct relation between the data series.

3.5. Stationary dominant periods and minima

The relations between the identified dominant periods in the SN, TSI-HS and TSI-LS series are shown in Table 1, where R is the autocorrelation of the wavelet spectrum.

In Table 2, we compare values of the stationary models $P(hsc, t)$, $P(lsc, t)$ and $P(snc, t)$ at minima corresponding to the solar activity minima determined by Usoskin et al. (2007). The grand minimum periods are calculated from the stationary models in Eqs. 9, 13 and 17 and are compared with *Spox* and *Spoy* maxima. The model $P(snc, t)$ computes a new Dalton sunspot minimum from approximately 2025 to 2050, the model $P(hsc, t)$ computes a new Dalton TSI minimum period (2035–2065), and the model $P(lsc, t)$ computes a new Dalton TSI minimum period (2045–2070).

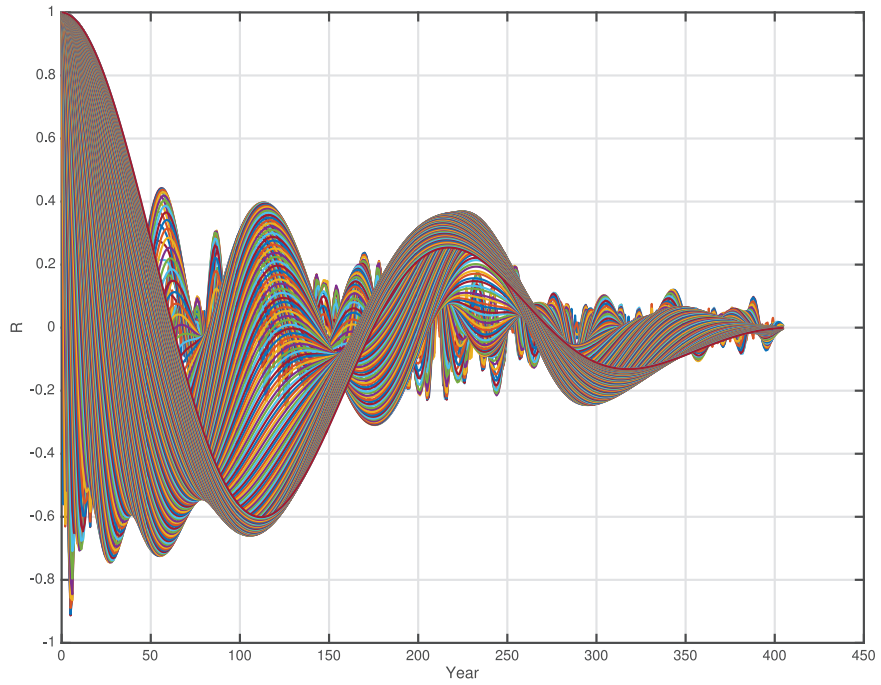

Fig. 12. Autocorrelations $Rsn(s, m)$ of the SN wavelet spectrum $Wsn(s, t)$ for $s = 0 \ldots 240$ and $m = 0 \ldots 400$.

Table 1
Identified stationary periods.

Data	Per,R	Per,R	Per,R	Per,R	Per,R	Per,R	Per,R	Per,R	Per,R
Planet	*PJ*	*PS*	*P*(55)	*PU*	*P*(110)	*P*(125)	*PN*	*P*(210)	*P*(373)
period (yr)	11.862	29.447	2*PU*/3	84.02	4*PU*/3	3*PU*/2	164.79	5*PU*/2	9*PU*/2
P(SPO)	*spoy*, 12	*spoy*, 29		*spoy*, 84			*spoy*, 165		
R=	0.98	0.95		0.90			0.90		
TSI-HS	*hs*, 11			*hs*, 84			*hs*, 164		
R=	0.55			0.65			0.70		
TSI-LS	*ls*, 11	*ls*, 29		*ls*, 83		*ls*, 125		*ls*, 210	*ls*, 373
R=	0.80	0.20		0.17		0.60		0.35	0.50
SN	*sn*, 11		*sn*, 55	*sn*, 86	*sn*, 110			*sn*, 210	
R=	0.73		0.43	0.35	0.40			0.36	

The SN model in Eq. 17 is a simplified model. This model has a minimum $P(snc, t) \leq -0.5$ in 1907–1931, which is not shown in the table. The HS model from Eq. 9 has grand minima in 1200–1230 and 1876–1887, which are not shown in the table. For this model, the Dalton minimum is less deep. The LS model from Eq. 13 has the maximum index $P(lsc, t) \geq 0.5$ for the periods (1093–1134), (1198–1241), (1351–1357), and (1945–2013) and the grand maximum index $P(lsc, t) \geq +1.0$ for the periods (1582–1610) and (1959–2001).

4. Discussion

The study of the TSI variability is based on the TSI-HS data series from 1700 to 2013 A.D., the TSI-LS data series from 1000 to 2100 A.D., sunspot data series from 1610–2015 A.D. and a solar barycenter orbit data series from 1000–2100 A.D. The results are, however, limited by how well they represent the solar physics and how well the methods are able to identify the periods in the data series. The investigation is based on a new method. The data series are transformed into a wavelet spectrum to separate periods, and the wavelets are transformed into a set of autocorrelations to identify the first periods, subharmonic periods and coincidence periods. The identified stationary periods in the TSI and SN data series are supported by the close relations with the well-known solar position periods and documented solar minimum periods. The solar orbit data will then provide a stable and computable reference. We have used the Dalton minimum (1790–1820) as a reference period because our two TSI data series and the SN data series cover this minimum. We observe that maxima in *SPOx* and *SPOy* correspond to minima in $SPO\ddot{x}$ and $SPO\ddot{y}$, which means maximum negative acceleration. We use $P(spoxc, 84, max) = 1797$ as a time of reference. This is close to Uranus perihelion (1798) and Neptune aphelion (1804), which indicates a possible relation between the distance to these planets and the Dalton minimum.

4.1. TSI-HS variability

The dominant periods in the TSI-HS variability are related to the large planets, as shown in Table 1. The correlation between the TSI-HS data series and the identified dominant wavelet periods $Whs(49, t) + Whs(86, t) + Whs(164, t)$ is estimated to be $R = 0.93$. The dominant periods $P(hs, 11)$ and $P(hs, 49)$ have a time-variant phase and represent mean estimates. A possible source of the $P(hs, 49)$ period is the interference between the Saturn period $P(hs, 29)$ and the Neptune period $P(hs, 164)$. The periods $P(hs, 84)$ and $P(hs, 164)$ have a stable period and phase in the time period from 1700 to 2013. The TSI-HS data series from 1700 is too short for a reasonable estimate of $P(hs, 164)$. A possible alternative is a coincidence resonance between the subharmonic period $P(hs, 2 * 84 = 168)$ and the 164-year Neptune period.

Table 2
Minimum periods from deterministic models.

Data series	Oort	Wolf	Spörer	Maunder	Dalton	Next
Minima periods:	1010-1070	1270-1340	1390-1550	1640-1720	1790-1820	
$P(spocx, 84)$ max	1043	1296	1462	1630	1797	2049
$P(spocy, 84)max$	1068	1326	1487	1654	1820	2073
HS model period	1033–1055	1369–1389	1537–1554	1706–1721	1796–1830	2035–2065
$P(hsc, t)$	< -1.0	< -1.0	< -1.0	< -1.0	< 0	< -0.7
HS model min	1040	1337	1547	1714	1810	2049
$P(hsc, t)$ min	−1.30	−1.23	−1.87	−1.13	−0.33	−1.0
LS model period	1014–1056	1276–1301	1404–1435	1657–1689	1785–1810	2045–2070
$P(lsc, t)$	< -1.0	< -0.5	< -1.0	< -0.7	< -0.7	< -0.7
LS model min	1035	1289	1418	1672	1796	2060
$P(lsc, t)$ min	−1.40	−0.62	−1.20	−0.91	−0.81	−0.79
SN mode l period	1019–1032	1242–1256	1467–1478	1693–1699	1802–1820	2025–2050
$P(snc, t)$	< 1.0	< -1.0	< -1.0	< -1.0	< -0.5	< -0.5
SN model min	1026	1249	1473	1696	1811	2035
$P(snc, t)$ min	−1.7	−1.18	−1.13	−1.04	−0.79	−0.84

The model $P(hsc, t)$ computes the deterministic oscillations in the TSI-HS variability. Table 2 shows that $P(hsc, t)$ computes a minimum in the period from 1796 to 1830. In the same time period, $P(spox, 84)$ and $P(spoy, 84)$ have maxima in 1797 and 1820. A close relation between the minimum of the period $P(hs, 84)$ and the maximum states of $P(spox, 84)$ and $P(spoy, 84)$ is observed.

The identified wavelet stationary periods $Whs(84, t)$ and $Whs(164, t)$ are transformed to a simplified model in Eq. 9, which produces a simplified deterministic TSI-HS data series from 1000 to 2100 A.D. The computed results in Table 2 show a close relation between the $P(spox, 84)$ maxima periods and minimum sunspot periods. The stationary model predicts minima in 1880 and 1960, which is observed in the TSI-HS reconstruction (Fig. 3). The model in Eq. 9 identifies three additional $P(hsc, t) \leq 0$ minimum periods, which are not shown in Table 2. These periods are (1296–1313), (1629–1656) and (1962–2002). The last period had a $P(hsc, t) = -0.40$ state in 1979. The model estimates a minimum $P(hsc, t) \leq -0.5$ in the period (2030–2065), a grand minimum $P(hsc, t) \leq -1.0$ period (2044–2054) and a local minimum irradiation state in approximately 2050. These estimates support the identification of Uranus, in resonance with Neptune, as the major cause of TSI-HS variability.

The implication of this result is a chain of events between the solar inertial motion due to the large planets and the TSI-HS variability. The SPO period $P(spoy, 84)$, controlled by the 84-year Uranus period, may serve as a reference for the TSI-HS variability.

4.2. TSI-LS variability

The TSI-LS variability is influenced by the periods from the large planets, as shown in Table 1. The major variability is, however, influenced by the long stationary periods $P(ls, 125)$ and $P(ls, 210)$. A stationary period in a data series has a stationary source. The autocorrelations in Fig. 8 indicate 3/2 and 5/2 combination resonances to $P(ls, 84)$, which produce the stationary periods $P(ls, 3 * 84/2 = 126)$ and $P(ls, 5 * 84/2 = 210)$. The same stationary deterministic periods produce a new set of subharmonic periods $P(ls, n{*}126)$ and $P(ls, n{*}210)$ for $n = 1, 2, 3$. When $P(ls, 125)$ and $P(ls, 210)$ are related to the stationary Uranus period $P(U, 84.02)$, they will produce a set of subharmonic stationary periods. The period $P(ls, 3 * 84/2 = 126.03)$ will produce the subharmonic periods $P(ls, 2 * 126.03 = 252.06)$, $P(ls, 3 * 126.03 = 378.09)$, $P(ls, 4 * 126.03 = 504.12)$, $P(ls, 5 * 126.03 = 630.15)$ and $P(ls, 6 * 126.03 = 756.18)$. The period $P(ls, 5 * 84/2 = 210.05)$ will produce the subharmonic periods $P(ls, 2 * 210.05 = 420.1)$ and $P(ls, 3 * 210.05 = 630.15)$, which indicate that $P(ls, 126.03)$ and $P(ls, 210.05)$ have a coincidence resonance in periods of approximately 630 years (Nayfeh and Mook, 2004; Ghilea, 2014).

The TSI-LS data series was reconstructed by Velasco Herrera et al. (2015), who performed a wavelet analysis of their TSI-PMOD and TSI-ACRIM reconstructions for the years 1000–2100 A.D. and discovered periods of 11 ± 3, 60 ± 20, 120 ± 30 and 240 ± 40 years. They interpreted the 11-year period as the Schwabe cycle and the 60-year period as the Yoshimura-Gleissberg cycle, which is associated with solar barycentric motion. They associated the 120-year period with solar magnetic activity (Velasco Herrera, 2013), and the 240-year period was associated with barycentric motion, as discovered by Jose (1965). They concluded that the negative phase of the 120-year period coincides with the grand minima, and the positive phase of the 120-year period coincides with the grand maxima. The next minimum should appear between 2010 and 2070 according to this interpretation. Long periods were also identified by McCracken et al. (2014), who analyzed ^{10}Be from cosmic ray variations over the past 9400 years by a Fourier spectrum analysis and identified three related period pairs (65 and 130), (75 and 150), and (104 and 208) in addition to periods of 350, 510 and 708 years. The identified 210-year period is known as the de Vries/Suess period. It was identified as a stationary period of approximately 210 years in the radiocarbon dating of pine tree rings of the past 8000 years (Suess, 1980).

The identified periods in this investigation support the studies by Suess (1980); Velasco Herrera et al. (2015) and McCracken et al. (2014). The new information reveals that all long periods in the TSI-LS variability are traced to the Uranus period $P(U, 84.02)$. This study confirms that the TSI-LS variability is dominated by deterministic periods and explains why the identified periods from Suess (1980) and McCracken et al. (2014) are found in series with lengths of 8000 and 9400 years.

Identifying the stationary periods in TSI variability can provide information about future irradiation variability and expected long-term climate variation. The minima computed from the deterministic model (Eq. 13) show a close relation between the solar grand minimum periods and the computed minimum periods from the model (Table 2). From this deterministic model, we may expect a new TSI minimum $P(lsc, t) \leq -0.5$ for the period 2040–2080, a Dalton state level $P(lsc, t) \leq -0.7$ in the time period 2048–2068 and a minimum state $P(lsc, t) = -0.9$ at approximately 2060.

4.3. Sunspot variability

Analysis of the sunspot data series from 1610 identified the first dominant periods $P(sn, 11)$, $P(sn, 55)$, $P(sn, 110)$ and $P(sn, 210)$, as shown in Table 1. The period $P(sn, 11)$ is a mean estimate from a time-variant phase. This may be explained by the analyses of Scafetta (2012a) and Solheim (2013), which show that the 11-year

Schwabe period can be resolved into 4 periods, all related to planetary periods (Scafetta, 2014a).

The wavelet spectrum in Fig. 11 shows that the period $P(sn, 55)$ has a time-variant amplitude that is controlled by the period $P(sn, 110)$. The stationary first period $P(sn, 11)$ is related to the Jupiter period $P(J, 11.862)$ and produces the subharmonic periods $P(sn, 5 * 11.862 = 59.31)$, $P(sn, 2 * 59.31 = 118.62)$ and $P(sn, 4 * 59.31 = 237.24)$.

The periods have a combination resonance to the Uranus period $P(U, 84.02)$. The autocorrelation spectrum in Fig. 12 shows that the period $P(sn, 55)$ has a 2/3 combination resonance to the period $P(sn, 84)$. This finding indicates that the identified period $P(sn, 55)$ is a stationary period that is controlled by the Uranus period $P(U, 84.02)$ from the 2/3 relation $2 * 84.02/3 = 56.01$ years. This first stationary period is expected to produce a new set of subharmonic periods of approximately $2 * 56 = 112$ and $4 * 56 = 224$ years. The identified period $P(sn, 210)$ has a 5/2 combination resonance to the Uranus period $P(U, 84.02)$ by the relation $5 * 84.02/2 = 210.05$ years. Table 1 shows a close relation between the identified TSI period $P(hs, 11)$, $P(ls, 11)$, the sunspot period $P(sn, 11)$ and the Jupiter period $P(J, 11.862)$. This study has demonstrated that the Uranus period $P(U, 84.02)$ introduces a deterministic TSI period of approximately $5 * 84/2 = 210.05$ years, a deterministic sunspot period of approximately $4(2 * 84.02/3) = 224.05$ years and a mean coincidence period of 217 years.

The sunspot data series has been investigated for decades. Schwabe (1844) proposed Jupiter as a source for $P(sn, 11)$, and Ljungman (1879) presented the theory that the long-term herring biomass fluctuation was related to a 111-year sunspot cycle. Scafetta (2012a) found that the 11-year triplet generated beat periods at approximately 115, 61 and 130 years in addition to a millennial large beat cycle at approximately 983 years. This explained the Ort, Wolf, Maunder and Dalton minima and forecasted a new deep minimum during 2020–2045. The 210-year de Vries/Suess period is also related to a climate cycle (Suess, 1980). A bicentennial TSI period of 200 ± 70 years was also determined by Abdussamatov (2013), who forecasted a TSI minimum around the year 2043 ± 11 and a deep cooling starting in the year 2060 ± 11, representing the 19th Little Ice Age in the past 7500 years.

The new information from this study is that the 210-year de Vries/Suess period, which is identified as a deterministic period in the TSI-LS and the sunspot data series, has its minimum at a phase difference of 0.35π(rad/year) from the SPOx maximum in 1797, which coincides with the Uranus perihelion. This shows that they are controlled by the same 84-year Uranus period.

This study shows that solar variability and TSI variability have deterministic coincidence periods of approximately 11 and 210–220 years. The deterministic model of the solar variability indicates that we may expect a new sunspot solar variability minimum $P(snc, t) \leq -0.5$ in the period from approximately 2025 to 2050, a Dalton level minimum $P(snc, t) \leq -0.7$ in the period from approximately 2030 to 2040 and a minimum state $P(snc, t) = -0.84$ in approximately 2035.

4.4. Possible explanation

This study of long solar variable data series has shown that the four large planets are the source of the solar position variability, the TSI variability, and the sunspot variability. In this chain of events, we may understand the solar dynamo oscillation as a coupled oscillator, forced by the GOs between the large planets and the Sun. The mutual GOs that exists between the four large planets and the solar position oscillation controls the transfer of angular momentum between the planets and the solar dynamo (Sharp, 2013).

Analysis of the solar position oscillation shows that the 84-year Uranus period $P(spox, 84)$ may serve as a reference for the forced GOs influence on the solar dynamo. The actual influence of SPO gravity on the solar dynamo is more complex.

Because the direct gravitational effect is small (Scafetta, 2012b), an amplification mechanism is required to produce the TSI variations. Several mechanisms for amplification have been proposed: a nonspherical shape of the tachocline (Abreu et al., 2008), the two meridional circulating magnetic waves (Shepherd et al., 2014; Zharkova et al., 2015), the tidal massage of the solar center resulting in greater nuclear energy production (Scafetta, 2012b), movement of elements near the center of the Sun (Wolf and Patrone, 2010; Cionco and Soon, 2015) or reconnection of magnetic field lines, which creates magnetic bubbles (Granpierre, 2015). A sudden loss of angular momentum from solar rotation to solar and planetary orbits may cause variations in differential rotation that modulate the dynamo, which generates a magnetic field and sunspot variations (Blizard, 1981). A phenomenological model proposed by McIntosh et al. (2014a); McIntosh and Leamon (2014b) and McIntosh and Leamon (2015), which explains the deep minima, requires a modulation of the solar differential rotation that may be a result of the transfer of angular momentum as proposed here. Transfer of angular momentum between the rotation of the Sun and the orbit of the planets is possible because of the wobble of the Sun. The axis of rotation is tilted with respect to the axes of the orbital plane, and the shape of the Sun is elliptical in the polar directions. Because the Earth also moves inside the solar wind, modulation of the solar wind by the four large planets may also be directly felt by the Earth, in addition to the exchange of angular momentum resulting in faster or slower rotation, which modulates the climate (Mörner, 2010).

Other studies have identified stationary periods in the solar dynamo. Duhau and de Jager (2008) analyzed the variation of the solar-dynamo magnetic field since 800 and identified periods of approximately 11, 22, 88 and 208 years. Shepherd et al. (2014) and Zharkova et al. (2015) identified two dynamo waves that show periods of 320 to 400 years, with an amplitude modulation in the range of 20 to 24 years. These periods are similar to some of the identified periods in Table 1. The new information from this study is that the identified solar dynamo periods have a deterministic relation to the stationary periods from the four large planets, the TSI variability and the sunspot variability. The stationary solar dynamic periods explains why the 125-year TSI-LS period produces a subharmonic period of approximately 3∗125 or 375 years.

5. Conclusions

A better understanding of the deterministic properties of the TSI variability is critical for understanding the cause of irradiation variability and how the TSI irradiation will contribute to the natural climate variation on the Earth. In this study, we have identified stationary periods in the TSI-HS data series from 1700–2013 A.D., in the TSI-LS data series from 1000–2100 A.D. and in the sunspots data series from 1610–2015 A.D. The identified stationary periods are related to the SPO and the periods from the four large planets. The results show that the TSI and sunspot data series variability have stationary oscillating periods that are controlled by the GOs from the large planets Jupiter, Saturn, Uranus and Neptune. The identified periodic relation between the solar system oscillation and the TSI variability indicates a chain of events between the solar system gravity force oscillation and the TSI variability. A possible chain of events is that the GOs between the Sun and the large planets influences the solar dynamo oscillation, which produces the TSI variability and the sunspot variability.

This study demonstrates that the major TSI variability and sunspot variability are controlled by the 12-year Jupiter period and

the 84-year Uranus period. The 11-year sunspot period is a mean estimate from a time-variant phase, which can be resolved into 4-periods, all related to planetary periods (Scafetta, 2014a). The TSI data series from 1700 has a variability that is controlled by the 12-year Jupiter period and the 84-year Uranus period. The TSI data series from 1000 A.D. has a stationary dominant period of approximately 125 years, which is controlled by a 3/2 resonance to the 84-year Uranus period, and a 210-year period by a 5/2 resonance to the 84-year Uranus period. The stationary periods of approximately 125 and 210 years introduce a new set of deterministic subharmonic periods. This study confirms the deterministic relation between 210-year variability and TSI variability, which is known as the 210-year de Vries/Suess period (Suess, 1980).

The identified stationary periods in TSI variability and sunspot variability are transformed into deterministic models of TSI oscillation and sunspot oscillation. The close relation between the computed deterministic model minima and the known minimum periods since 1000 A.D. confirms the identified periods from this study. The deterministic models of SN and TSI variability computes a new Dalton-type sunspot minimum from 2025 to 2050 and a new Dalton-period-type TSI minimum from approximately 2040 to 2065.

Acknowledgments

We thank N. Scafetta and V. M. Velasco Hererra for providing the data sets for TSI that we used in this investigation. We also thank the anonymous referees for valuable suggestions, which helped us to improve the manuscript.

References

Abdussamatov, H., 2013. Grand minimum of the total solar irradiance leads to the little ice age, nestor-istorya, st. petersburg, october 2013, ISBN 978-5-44690-122-7-246 p. In: Russian, translated as SPPI Original Paper, Nov 25, 2013.

Abreu, J.A., Beer, J., Steinhilber, F., Tobias, S.M., Weiss, N.O., 2008. For how long will the current grand maximum of solar activity persist? Geophys. Res. Lett. 35, L20109.

Blizard, J.B., 1981. Solar motion and solar activity. Bull. Am. Astron. Soc 13, 876.

Charbonneu, P., 2010. Dynamo model of the solar cycle. Living Rev. Sol. Phys. 7, 3. www.livingreviews.org/lrsp-2010-3.

Charvátová, I., Hejda, P., 2014. Responses of the basic cycles of 178.7 and 2402 year in solar-terestrial phenomena during the holocene. Pattern Recognit. Phys. 2, 21–26.

Cionco, R.G., Soon, W., 2015. A phenomenological study of the timing of solar activity minima of the last millennium through a physical modeling of the sun–planets interaction. New Astron. 34, 164–171.

Clette, F., Svalgaard, L., Vaquero, J.M., Cliver, E.W., 2014. Revisiting the sunspot number. In: The Solar Activity Cycle, V 53 Space Sciences Series of ISSSI, pp. 35–103.

Daubechies, I., 1992. Ten lectures of wavelet. SIAM J. Math. Anal. 24, 499–519.

Duhau, S., de Jager, C., 2008. The solar dynamo and its phase transition during the last millennium. Sol. Phys. 250, 1–15.

Eddy, J.A., 1976. The maunder minimum. Sci. 192, 1189–1202.

Eddy, J.A., 1983. The maunder minimum a reappraisal. Sol. Phys. 89, 195–207. doi: 10007/BF00211962.

Fairbridge, R.W., Shirley, J.H., 1987. Prolonged minima and the 179-yr cycle of the solar inertial motion. Sol. Phys. 110, 191–220.

Foukal, P., Bernasconi, P., Fröhlich, C., 2009. Recent anomalous TSI decrease not due to low polar facula and network areas: Time to broaden our view on solar luminosity variation? Bull. Am. Astron. Soc. 41, 827.

Fröhlich, C., Lean, J., 1998. The sun's total irradiance: Cycles, trends and related climate change uncertainties since 1976. Geophys. Res. Lett. 25 (23), 4377–4380.

Ghilea, M. C., 2014. Statistical distributions of mean motion resonances and near-resonances in multiplanetary systems. ArXiv:14102478G.

Gleissberg, W., 1958. The eighty-year sunspot cycle. J. Br. Astron. Assoc. 68, 148–152.

Gleissberg, W., 1965. The eighty-year solar cycle in auroral frequency numbers. J. Br. Astron. Assoc. 75, 227–231.

Granpierre, A., 1990. How is the sun working? Sol. Phys. 128, 3–6.

Granpierre, A., 1996. On the origin of solar periodicity. Astrophys. Space Sci. 243, 393–400.

Granpierre, A., 2015. The origin of solar activity: Local thermonuclear runaways in hot bubbles and their triggers. In: Mörner, N.-A. (Ed.), Planetary influence on the Sun and the Earth, and a modern book-burning. Nova publ, pp. 91–108. ISBN 978-1-63482-837-6.

Hassan, D., et al., 2016. Sunspots and ENSO relationship using markov method. J. Atmos. Sol. Terr. Phys. 137, 53–57. doi: dx.doi.org/10.1016/jastp.2015.11.017.

Hathaway, D.H., 2015. The solar cycle. Living Rev. Sol. Phys. 12 (4).

Hoyt, D.V., Schatten, K.H., 1993. A discussion of plausible solar irradiance variations, 1700-1992. J. Geophys. Res. 98, 18895–18906.

Hoyt, D.V., Schatten, K.H., 1998a. Group sunspot numbers: A new solar activity reconstruction. Sol. Phys. 179, 189–219.

Hoyt, D.V., Schatten, K.H., 1998b. Group sunspot numbers: A new solar activity reconstruction. Sol. Phys. 181, 491–512.

Hoyt, D.V., Schatten, K.H., Nesme-Ribes, E., 1994. The one hundredth year of rudolf wolfs death: Do we have the correct reconstruction of solar activity? Geophys. Res. Lett. 21, 2067–2070.

Hung, C.-C., 2007. Apparent relations between solar activity and solar tides caused by the planets. NASA/TM-2007-214817. Technical Memorandum.

de Jager, C., Duhau, S., 2011. The variable solar dynamo and the forecast of solar activity; influence on terrestrial surface temperature. In: Cossia, J.M. (Ed.), Global warming in the 21st Century. Nova Science Publishers, Inc. ISBN978-1-61728-980-4.

Jose, P.D., 1965. Sun's motion and sunspots. Astron. J. 70, 193–200. 1965.

Ljungman, A.V., 1879. Bidrag till lösningen af frågan om de stora sillfiskenas sekulära periodisitet. Tidskrift for Fiskeri 5, 257–268. (In Swedish).

Ljungquist, F.C., 2010. A new reconstrunction of temperature variability in the extra-tropical northern hemisphere during the last two millennia. Geogra. Ann. 92 A (3), 339–351.

Matlab, 2015. Matlab. Wavelet Toolbox. Users Guide. The Math Works Inc.

Maunder, E.W., 1890. Professor spoerer's researches on sun-spots. MNRAS 50, 251–252.

McCracken, K.G., Beer, J., Steinhilber, F., 2014. Evidence for planetary forcing of the cosmic ray intensity and solar activity throughout the past 9400 years. Sol. Phys. 289, 3207–3229. doi:10.1007/s11207-014-0510-1.

McIntosh, S.W., Leamon, R.J., 2014b. On magnetic activity band overlap, interaction, and the formation of complex solar active regions. ApJ 796. L19-24. doi: dx.doi.org/10.1088/2041-8205/796/1/L19.

McIntosh, S.W., Leamon, R.J., 2015. Deciphering solar magnetic activity: On gand minima in solar activity. Stellar Solar Phys. 1. Id.2. doi: 10.3389/fspas.2015.00002.

McIntosh, S.W., Wang, X., Leamon, R.J., et al., 2014a. Deciphering solar magnetic activity i. on the relationship between the sunspot cycle and the evolution of small magnetic features. ApJ 792, 12–30. doi:10.1088/0004-637X/792/1/12.

Mörner, N.-A., 2010. Solar minima, earth's rotation and little ice ages in the past and in the future the north atlantic-european case. Global Planet. Change 72, 282–293. doi:10.1016/j.gloplacha.2010.01.004.

Mörner, N.-A., Scafetta, N., Solheim, J.-E., 2015. The january 7 giant solar flare, the simultaneous triple planetary conjunction and additional records at tromsø, norway. In: Mörner, N.-A. (Ed.), Planetary infuence on the Sun and the Earth, and a modern book-burning. Nova publ, pp. 33–38. ISBN 978-1-63482-837-6.

Nayfeh, A.H., Mook, D.T., 2004. Nonlinear Oscillations. WILEY-VCH Verlag GmbH & Co. KGaA, Weinheim. ISBN-10:0-471-12142-8.

Ogurtsov, M.G., Nagovitsy, A., Kocharov, G.E., Jungner, H., 2002. Long-period cycles of the sun's activity recorded in direct solar data and proxies. Sol. Phys. 211, 371–394.

Peristykh, A.N., Damon, P.E., 2003. Persistence of the gleissberg 88-year solar cycle over the last ~12,000 years: Evidence from cosmogenic isotopes. J. Geophys. Res. Space Phys. 108. A1,pp.SSH 1-1, CiteID 1003. doi: 10.1029/2002JA009390.

Scafetta, N., 2012. Does the sun work as a nuclear fusion amplifier of planetary tidal forcing? a proposal for a physical mechanism based on the mass-luminosity relation. J. Atmos. Sol. Terr. Phys. 81, 27–40. doi:10.1016/j.jastp.2012.04.002.

Scafetta, N., 2012a. Multi-scale harmonic model for solar and climate cyclical variations through the holocene based on jupiter-saturn tidal frequencies plus the 11-year solar cycle. J. Atmos. Sol. Terr. Phys. 80, 296–311. doi:10.1016/j.jastp.2012.02.016.

Scafetta, N., 2012b. Does the sun work as a nuclear fusion amplifier of planetary tidal forcing? a proposal for a physical mechanism based on the mass-luminosity relation. J. Atmos. Sol. Terr. Phys. 81, 27–40. doi:10.1016/j.jastp.2012.04.002.

Scafetta, N., 2014a. The complex syncronization structure of the solar system. Pattern Recogn. Phys. 2, 1–19. doi:10.5194/prp 2-1-2014.

Scafetta, N., 2014b. Discussion of the spectral coherence between planetary, solar and climate oscillations: a reply to some critiques. Astrophys. Space Sci 354 (2), 275–299. doi:10.1007/s10509-014-2111-8.

Scafetta, N., Willson, R.C., 2014. ACRIM total solar irradiance satellite composite validiation versus TSI proxy models. Astrophys. Space Sci. 350 (2), 421–442. doi:10.1007/s10509-013-1775-9.

Schwabe, H., 1844. Sonnen-beobactungen im jahre 1843. Astron. Nachr. 21 (495), 233–236.

Sharp, G.J., 2013. Are uranus & neptune responsible for solar grand minima and solar cycle modulation? Int. J. Ast. & Astrophys. 3, 260–273. dx.doi.org/10.4236/ijaa.2013.33031.

Shepherd, S.J., Zharkov, S.I., Zharkova, V.V., 2014. Prediction of solar activity from solar background magnetic field variations in cycles 21-23. ApJ. 795 (1). Article id. 46,8 pp. doi: 10.1088/0004-637X/795/1/46.

Solanki, S.K., Usoskin, I.G., Kromer, B., Schüssler, M., Beer, J., 2004. Unusual activity of the sun during recent decades compared to the previous 11,000 years. Nature 431, 1084–1087.

Solheim, J.-E., 2013. The sunspot cycle length - modulated by planets? Pattern Recogn. Phys. 1, 159–164. doi:10.5194/prp 1-159-2013.

Soon, W., Connolly, R., Connolly, M., 2015. Re-evalutating the role of solar variability on northern hemisphere temperature trends since the 19th century. Earth-Sci. Rev. 150, 409.
Suess, H.E., 1980. The radiocarbon record in tree rings of the last 8000 years. In: Proc. of the 10th international Conference on Radiocarbon Dating, Bern and Heidelberg 1979, Radiocarbon, 22, pp. 200–209.
Usoskin, I.G., 2013. A history of solar activity over millennia. Living Rev. Solar Phys. 10 (1). URL(accessed 2014, 0530): http://www.livingreviews.org/lrsp-2013-1.
Usoskin, I.G., et al., 2014. Evidence for distinct modes of solar activity. As& A 562. L10. doi: 10.1051/0004-6361/201423391.
Usoskin, I.G., Solanki, S.K., Kovaltsov, G.A., 2007. Grand minima and maxima of solar activity: new observational constraints. A&A 471, 301–309.
Usoskin, I.G., Solanki, S.K., Schüssler, M., Mursula, K., Alanko, K., 2003. Millennium-scale sunspot number reconstruction: Evidence for an unusually active sun since the 1940s. Phys. Rev. Lett. 91, 211101.
Velasco, V.M., Mendoza, B., 2008. Assessing the relationship between solar activity and some large scale climatic phenomena. Adv. Space Res. 42, 866–878. doi:10.1016/j.asr.2007.05.050.
Velasco Herrera, V.M., 2013. In: Jorge, A., Perez-Peraza (Eds.), Homage to the discovery of cosmic rays, the meson-muon and solar cosmic rays. Nova publ., p. 469. Chap. 15.
Velasco Herrera, V.M., Mendoza, B., Velasco Herrera, G., 2015. Reconstruction and prediction of the total solar irradiance: From the medival warm period to the 21st century. New Astron. 34, 221–233.
Willson, R.C., 2014. ACRIM3 and the total solar irradiance database. Astrophys. Space Sci 352 (2), 341–352. doi:10.1007/s 10509-014-1961-4.
Wilson, I.R.G., 2013. The venus-earth-jupiter spin-orbit coupling model. Pattern Recognit. Phys. 1, 147–158. doi:10.5194/prp-1-147-2013-.
Wolf, C.I., Patrone, P.N., 2010. A new way that planets can affect the sun. Sol. Phys 266, 227–246. doi:10.1007/s11207-0101-9628-y.
Wolf, C.L., O'Donovan, A.E., 2007. Coupled groups of g-modes in a sun with a mixed core. ApJ. 661, 568–585.
Wolf, R., 1859. Extract of a letter to mr. carrington. MNRAS 19, 85–86.
Wolf, R., 1861. Abstract of his latest results. MNRAS 21, 77–78.
Zhao, J., Bogart, R.S., Kosovichev, A.G., Duvall Jr., T.L., Hartlep, T., 2013. Detection of equatorward meridional flow and evidence of double-cell meridional circulation inside the sun. ApJ 774, L29.
Zharkova, V. V., Shepherd, S. J., Popova, E., Zharkov, S. I., 2015. Heartbeat of the sun from principal component analysis and prediction of solar activity on a millennium timescale. www.nature.com/Scientific, 5, 15689, doi:10.1038/srep1569.